The Astrophysical Journal, 988:252 (23pp), 2025 August 1 https://doi.org/10.3847/1538-4357/ade80d
© 2025. The Author(s). Published by the American Astronomical Society.
OPEN ACCESS

SOFIA/HAWC+ Far-infrared Polarimetric Large Area CMZ Exploration Survey. V. The Magnetic Field Strength and Morphology in the Sagittarius C Complex

Roy J. Zhao[1,2,3], Mark R. Morris[3], David T. Chuss[4], Dylan M. Paré[4], Jordan A. Guerra[5], Natalie O. Butterfield[6], Edward J. Wollack[7], and Kaitlyn Karpovich[4,8,9]

[1] Kavli Institute for Cosmological Physics, The University of Chicago, 5640 S Ellis Ave., Chicago, IL 60637, USA; rzhaolx@uchicago.edu
[2] Department of Physics, The University of Chicago, 5720 S Ellis Ave., Chicago, IL 60637, USA
[3] Department of Physics & Astronomy, University of California, Los Angeles, 475 Portola Pl., Los Angeles, CA 90095, USA
[4] Department of Physics, Villanova University, 800 E. Lancaster Ave., Villanova, PA 19085, USA
[5] Cooperative Institute for Research in Environmental Sciences, University of Colorado, Boulder, CO 80309, USA
[6] National Radio Astronomy Observatory, 520 Edgemont Rd., Charlottesville, VA 22903, USA
[7] NASA Goddard Space Flight Center, Mail Code: 665, Greenbelt, MD 20771, USA
[8] Kavli Institute for Particle Astrophysics & Cosmology, P.O. Box 2450, Stanford University, Stanford, CA 94305, USA
[9] Department of Physics, Stanford University, Stanford, CA 94305, USA

Received 2025 February 21; revised 2025 June 11; accepted 2025 June 23; published 2025 July 29

Abstract

We present an analysis of the magnetic field strength and morphology in the Sagittarius C complex (Sgr C; G359.43-0.09) in the Milky Way's Central Molecular Zone (CMZ), using the 214 μm polarimetry data acquired with the High-resolution Airborne Wide-band Camera instrument on board the Stratospheric Observatory for Infrared Astronomy. We conduct a modified Davis–Chandrasekhar–Fermi analysis of individual clouds and find that the sky-plane magnetic field strength varies from highly turbulent regions having inferred strengths of $\sim$30 μG to regions of relatively uniform field orientation having strengths of $\sim$400 μG. Several hundred magnetic field pseudovectors in the Sgr C region were measured to trace the projected magnetic field orientation within cold molecular clouds, and as is the trend throughout the CMZ, they show a higher polarization fraction toward the periphery of the clouds. The magnetic field orientations suggest that outflows from active star-forming regions, such as the G359.43-0.10 extended green object and the protostellar source FIR-4 (G359.43+0.02), cause high turbulence in their vicinity. The magnetic field direction is found to be tangential to the surface of the Sgr C H II region, which displays spatial correspondence with two [C II] emission cavities reported in the H II region, signifying a compression front between the H II region and the surrounding dense clouds. Several other features in the vicinity of Sgr C, especially numerous nonthermal radio filaments and a diffuse source of X-ray emission to the immediate southwest of the H II region, are discussed with regard to the magnetic field measurements.

Unified Astronomy Thesaurus concepts: Galactic center (565); Interstellar medium (847); Infrared astronomy (786); Magnetic fields (994); Polarimetry (1278)

1. Introduction

The central half kiloparsec of the Milky Way disk, commonly referred to as the Central Molecular Zone (CMZ), is an ideal laboratory to study astrophysics in extreme environments given its high density, massive star formation, and complex structure (see M. Morris & E. Serabyn 1996; K. Ferrière et al. 2007; A. Bryant & A. Krabbe 2021; J. D. Henshaw et al. 2023; and references within). Apart from the extensively studied star formation and interstellar medium (ISM) properties, a strong magnetic field has also been found to permeate the CMZ (M. Tsuboi et al. 1985; T. N. LaRosa et al. 2005; M. Morris 2006; K. Ferrière 2009; M. R. Morris 2015; M. S. Akshaya & T. Hoang 2024; D. Paré et al. 2024; R. G. Tress et al. 2024), especially in dense clouds (F. Yusef-Zadeh et al. 1999; T. Pillai et al. 2015; P.-Y. Hsieh et al. 2018; N. O. Butterfield et al. 2024a, hereafter FIREPLACE I; X. Lu et al. 2024). The relatively strong magnetic field (0.1–1 mG) is said to counteract the gravitational collapse of clouds and contributes to the lower than expected star formation rate in this region given its high density (M. Morris 1993; D. T. Chuss et al. 2003; J. M. D. Kruijssen et al. 2014; M. R. Morris 2023), therefore of great interest to be studied.

In this paper, we use the results of the Far-Infrared Polarimetric Large Area CMZ Exploration (FIREPLACE) survey (PI: D. Chuss), a high-resolution dust polarimetry survey conducted at 214 μm, to study the magnetic field in the CMZ. As a common experimental probe of the sky-plane component of the magnetic field, dust polarimetry exploits the property that the spin axes of dust grains tend to be aligned with the magnetic field (B. G. Andersson et al. 2015). The measurement of polarized emission from clouds therefore reveals the alignment of dust grains within, indicating the sky-plane magnetic field component integrated along the line of sight (D. T. Chuss et al. 2003; B. G. Andersson et al. 2015).

There are several possible mechanisms that could be responsible for the field orientations deduced from dust polarimetry observations. As the magnetic field lines are anchored inside the molecular clouds, the field lines could be sheared by the clouds' internal motions (E. N. Parker 1979). In a differentially orbiting medium like the CMZ, the shear stretches the magnetic field into a primarily toroidal geometry observed in large scale (M. W. Werner et al. 1988; M. Wardle & A. Konigl 1990). The same effect can also be indicative of the direction of the internal shear within clouds on a smaller scale (D. K. Aitken et al. 1991, 1998; M. Morris et al. 1992;

Original content from this work may be used under the terms of the Creative Commons Attribution 4.0 licence. Any further distribution of this work must maintain attribution to the author(s) and the title of the work, journal citation and DOI.

G. Novak et al. 2000; D. T. Chuss et al. 2003; M. R. Morris 2015). Other candidates that can contribute to the magnetic field orientations, such as cloud compression, which occurs at the interface of expanding H II regions or supernova blast waves, tend to shape the field to be parallel to the compressive interface.

Indeed, a high-resolution magnetic field study, like the FIREPLACE survey, can benefit our understanding of many aspects of the CMZ, such as the magnetic field morphology within molecular clouds and within portions of low-density ISM occupied by the nonthermal radio filaments (NTFs; F. Yusef-Zadeh et al. 1984; M. Morris & F. Yusef-Zadeh 1985; I. Heywood et al. 2022; F. Yusef-Zadeh et al. 2022b). These NTFs are manifested as spatially extended synchrotron emission from relativistic electrons constrained to diffuse along a magnetic flux tube. The NTFs within the CMZ are generally oriented perpendicular to the Galactic plane, which implies a large-scale vertical magnetic field pervading the Galactic center (GC), thereby pointing to the existence of an organized intercloud magnetic field (M. Morris & E. Serabyn 1996; I. Heywood et al. 2022). Furthermore, E. Serabyn & M. Morris (1994) argued that turbulent instabilities at the H_2/H II interface could mix two orthogonal magnetic field systems inside and outside that interface, which facilitates magnetic field line reconnection. Such a phenomenon can boost free electrons in the ISM to relativistic velocities, thereby forming NTFs as those electrons diffuse along the magnetic field lines in the intercloud ISM (E. Serabyn & M. Morris 1994; M. Morris 1996; D. T. Chuss et al. 2003). In addition, many other hypotheses have been offered to account for the NTFs (see references in M. Morris 1996; F. Yusef-Zadeh & A. Königl 2004; S. Boldyrev & F. Yusef-Zadeh 2006; W. E. Banda-Barragán et al. 2016, 2018; F. Yusef-Zadeh & M. Wardle 2019). For example, an alternative hypothesis for generating relativistic electrons that does not directly involve magnetic fields invokes diffusive shock acceleration where stellar winds from massive young stars impact relatively dense interstellar material (R. Rosner & G. Bodo 1996).

Previous studies of the GC magnetic field, including those using the Submillimeter Polarimeter for Antarctic Remote Observations (G. Novak et al. 2003), Planck (Planck Collaboration et al. 2015), the Polarized Instrument for the Long-wavelength Observation of the Tenuous ISM (A. Mangilli et al. 2019), and the Atacama Cosmology Telescope (Y. Guan et al. 2021), have focused on the large-scale magnetic field, with typical resolutions $\gtrsim 1'$. These works reported a largely uniform magnetic field that permeates the CMZ, and is oriented at a $\sim 20°$ angle with respect to the Galactic plane. However, conclusions made from these surveys remain on a global level, since the spatial resolution of these surveys does not generally resolve the internal structure of individual molecular clouds. High-resolution surveys conducted on subregions within the CMZ, such as those reported by D. T. Chuss et al. (2003) and X. Lu et al. (2024), found a correlation between the magnetic field orientation and molecular cloud density, although they do not have enough coverage to cover a sufficiently large portion of the CMZ to draw global conclusions. Along the same line in Sgr C, J. Bally et al. (2025) studied the magnetic field inside the prominent H II region using the JWST-NIRCam images. With the FIREPLACE survey data set, a recent study by D. M. Paré et al. (2025; or FIREPLACE IV) demonstrated the advantage of studying the magnetic field orientation in the CMZ using data sets with both high resolution and large coverage.

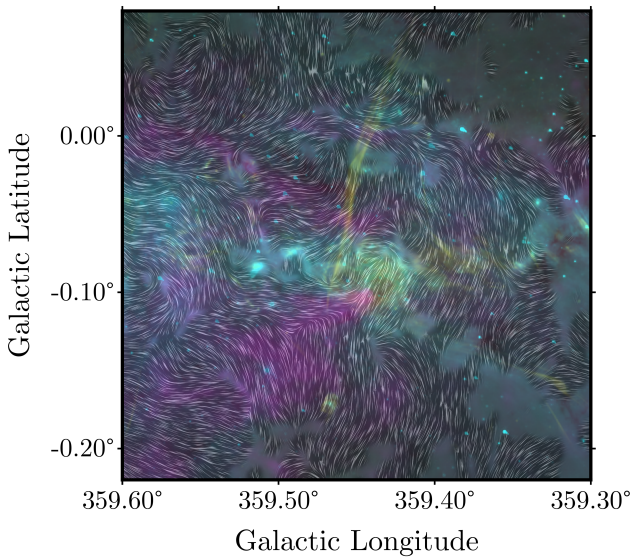


Figure 1. A tricolor view of the Sgr C complex with the Spitzer/IRAC 8 μm image in cyan (S. Stolovy et al. 2006), the Herschel/SPIRE 250 μm image in magenta (S. Molinari et al. 2010), and the MeerKAT/L-Band 20 cm image in yellow (I. Heywood et al. 2022), overlaid with an LIC rendition of the magnetic field measurements reported by D. Paré et al. (2024). The main structures, including the Sgr C H II region, the Sgr C NTF, FIR-4, and the 100 pc ring, are highlighted in Figure 2.

In this paper, we focus on studying the magnetic field within one of the subregions in the CMZ—the Sgr C complex. Sgr C was initially reported as one of the most prominent H II regions in the GC (D. Downes & A. Maxwell 1966), and it was later detailed by H. S. Liszt (1985) and H. S. Liszt & R. W. Spiker (1995), who noted the presence of a prominent NTF apparently connected to the H II region. Figure 1 portrays this region at multiple wavelengths overlaid with a line integral contour (LIC; B. Cabral & L. C. Leedom 1993) image to represent the magnetic field direction made by measurements reported by D. Paré et al. (2024; or FIREPLACE III). Figure 2 shows a simplified schematic diagram of Sgr C to highlight the important structures within.

The large-scale astrogeography of Sgr C is also of particular interest and may be crucial in reaching a full understanding of the global structure of the CMZ. Many studies found that the Sgr C complex resides on the projected western vertex of a dust ring associated with the X_2 orbit due to the Galactic bar potential (S. Molinari et al. 2011; M. R. Krumholz & J. M. D. Kruijssen 2015; M. C. Sormani et al. 2018; J. M. Salas et al. 2020). Through the lens of simulations, M. C. Sormani et al. (2024) and R. G. Tress et al. (2024) alternatively described the formation of the ring as a result of the particular gas dynamics in the Galactic bar, where shocks and magnetic field are also considered in these computations. Therefore, this theory places Sgr C and its positive-longitude counterpart, Sgr B2, at the two interaction sites of X_1–X_2 orbits, located at both projected ends of the nuclear stellar disk. Meanwhile, the Mopra survey (P. A. Jones et al. 2012) revealed a significant amount of shock tracers (SiO and HNCO) within the Sgr C complex. The widely distributed shock tracers are presumably induced by the X_1–X_2 orbit collision. The exact role of this collision is yet unclear since it can either compress the clouds and provoke star formation or

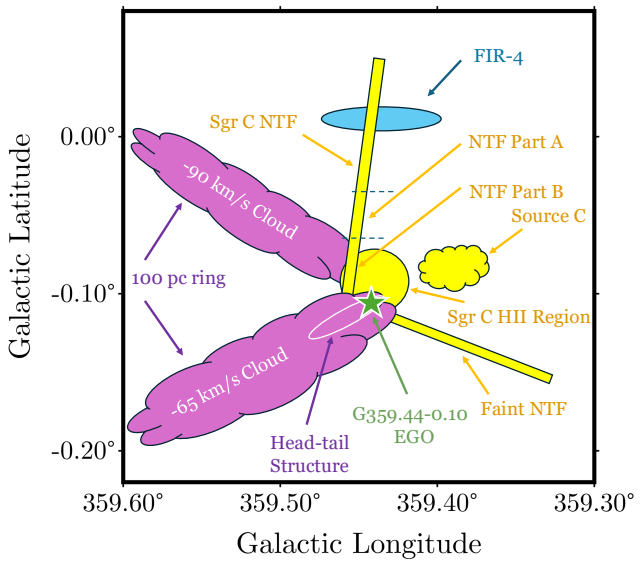


Figure 2. Schematic diagram of the main features within the Sgr C complex on the sky-plane, including FIR-4 (blue ellipse), the major molecular clouds detected in far-IR (purple clouds denoted by their measured velocities), the Sgr C H II region and NTF detected in radio continuum (yellow circle and long, vertical rectangle, respectively), the G359.44-0.10 EGO (S. Kendrew et al. 2013; green star), and the radio and mid-IR structure known as source C (yellow cloud). The velocities of the molecular clouds depicted in magenta are obtained using the molecular line observation of the 3 mm Mopra survey reported by P. A. Jones et al. (2012), detailed in Section 4.2.

increase turbulence and thereby inhibit star formation. As magnetic field measurements could reveal information about the large-scale turbulence of dense clouds, a thorough study of the magnetic field morphology within the Sgr C complex may provide improved characterization of a region subjected to large-scale shocks and how star formation enters the picture in such a region.

In this paper, we study the magnetic field measurements from the FIREPLACE survey within the Sgr C complex, in the context of other known structures in this region. The paper is organized as follows. In Section 2, we briefly describe the FIREPLACE survey. In Section 3, we present analyses of the Sgr C magnetic field measured in 214 μm. In Section 4, we use multiwavelength observations to investigate numerous intriguing structures in the Sgr C region where the magnetic field has apparently become manifested. In Section 5, we present a detailed examination of several features in which the magnetic field is likely playing an important role. We finally summarize our conclusions in Section 6. Throughout this paper, we adopt 8.2 kpc as the distance to the GC (GRAVITY Collaboration et al. 2019).

2. Observations and Data

The 214 μm intensity and polarization results presented in this paper utilize the second data release of the FIREPLACE survey described in FIREPLACE III. The data were acquired using High-resolution Airborne Wide-band Camera (HAWC +; D. A. Harper et al. 2018), an imaging polarimeter on board the Stratospheric Observatory for Infrared Astronomy (SOFIA) telescope. The complete survey, including the first data release (FIREPLACE I), covers the inner $1.^{\circ}5$ of the CMZ with a spatial resolution of $19.''6$. We refer interested readers to FIREPLACE III for full details of the observations and data reduction.

In this paper, the inferred magnetic field orientations represent the component of the magnetic field projected onto the plane of the sky and integrated along the line of sight. Additionally, we assume that the B-RAT dust grain alignment mechanism dominates in the Sgr C complex. Therefore, the magnetic field orientations are obtained by rotating the polarization orientations by 90° (B. G. Andersson et al. 2015). For a full visual representation, the length of the magnetic field pseudovectors presented in this paper is scaled to be proportional to the debiased polarization fraction, defined by

$$p = \sqrt{p_m^2 - \sigma_p^2}, \quad (1)$$

where p_m is the measured polarization fraction, and σ_p is the associated uncertainty.

Throughout this paper, we consider only those measurements that meet the conservative SOFIA/HAWC+ selection criteria: a polarization signal-to-noise ratio of $p/\sigma_p > 3$; a polarization fraction of $p < 50\%$; and a signal-to-noise ratio of the total intensity of $I/\sigma_I > 200$ (M. S. Gordon et al. 2018).

3. Magnetic Field in the Sgr C Complex

3.1. Overview

Figure 3 presents the 214 μm magnetic field measurements reported by FIREPLACE III as pseudovectors superposed on the Stokes I intensity image in the Sgr C region. A similar pseudovector representation of the magnetic field measurements is adopted throughout this paper. The 214 μm emission is dominated by thermal emission from dust in molecular clouds, including the $-90\,\mathrm{km\,s^{-1}}$ cloud in the north, the $-65\,\mathrm{km\,s^{-1}}$ cloud in the south, and FIR-4. Throughout the extended region surrounding Sgr C, the 214 μm polarization measurements that satisfy the selection criteria are clearly present with high significance throughout the far-IR-bright emission region. Measurements in faint regions do not commonly pass the selection criteria, owing either to low signal-to-noise ratio in either or both total intensity or polarization fractions, as outlined in Section 2. Pseudovectors in faint regions can be contaminated by residual systematic effects and/or confused by unrelated emissions originating outside the CMZ (D. T. Chuss et al. 2019; FIREPLACE I). However, in our field of view, our conservative selection criteria have largely mitigated such issues.

Throughout this paper, we compare our 214 μm magnetic field orientations to the 850 μm James Clerk Maxwell Telescope (JCMT) magnetic field orientations reported by X. Lu et al. (2024), depicted in orange in Figure 3. The magnetic field measurements of X. Lu et al. (2024) were obtained with a spatial resolution similar to that in FIREPLACE III and were produced under a similar set of cutoff thresholds. From Figure 3, the 850 μm magnetic field orientations do not generally agree with those at 214 μm. It is likely that, given the large difference in the survey wavelengths, these two studies sample different regimes of dust temperature along the line of sight (see, e.g., the dust temperature study reported by M. J. Hankins et al. 2017).

As was pointed out in FIREPLACE I and FIREPLACE III for other portions of the CMZ, the polarization fraction exhibits an anticorrelation with 214 μm intensity. That is, the

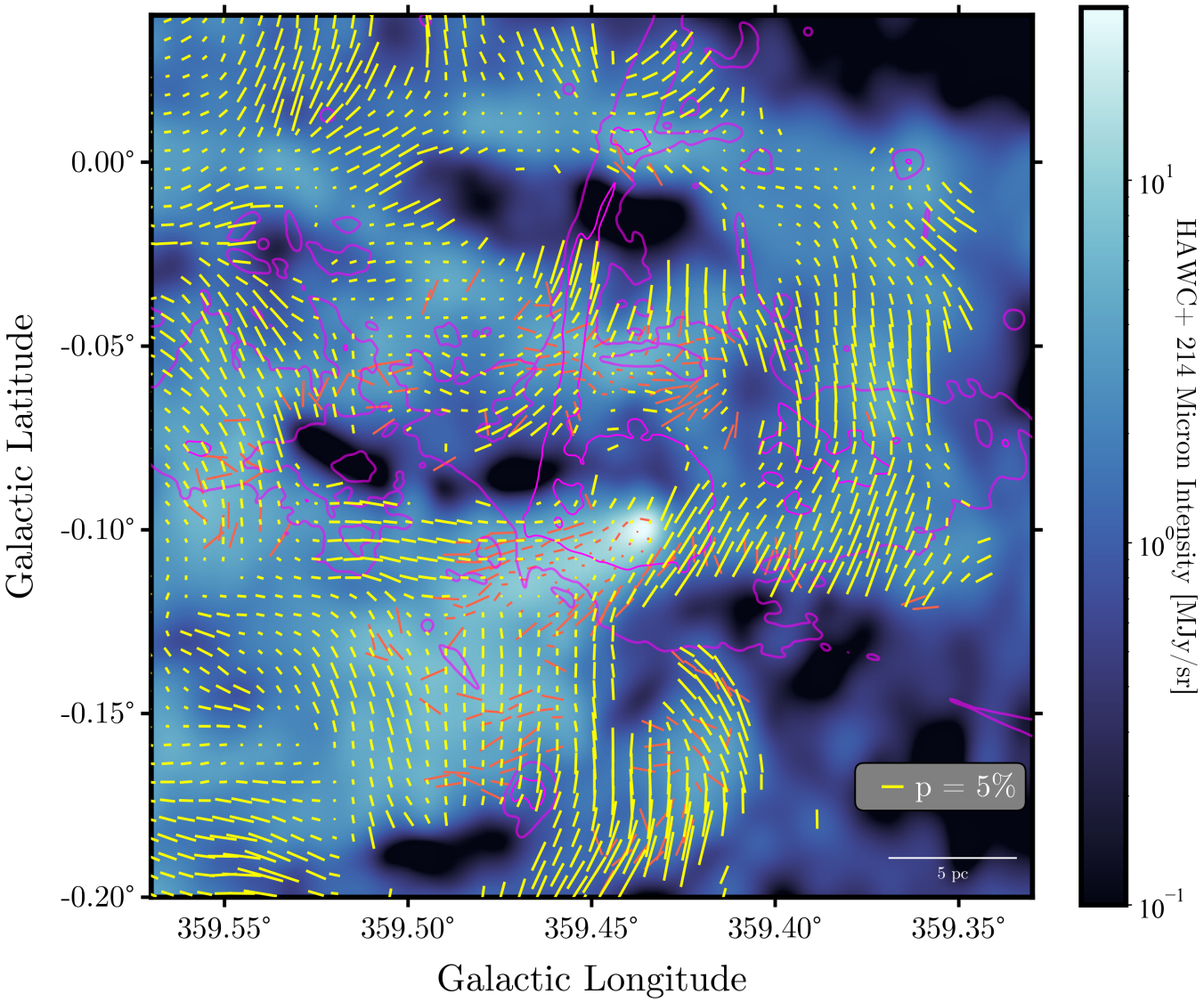


Figure 3. The FIREPLACE magnetic field pseudovectors in the Sgr C complex, displayed with the 214 μm intensity image in the background, rendered using measurements of D. Paré et al. (2024). The yellow dashes are the 214 μm magnetic field pseudovectors made using Nyquist sampling at the HAWC+ beam size, which fulfill the selection criteria described in Section 2. The length of the vectors is scaled by their polarization fraction. The legend in the lower right corner denotes the length of a 5% polarized pseudovector. The magenta contours are made from the MeerKAT/*L*-band observation of I. Heywood et al. (2022) at levels 0.0004 and 0.002 Jy beam^{-1}, with the brighter contour indicating higher-intensity level. The orange dashes are the JCMT/POL2 magnetic field detections at 850 μm (X. Lu et al. 2024). The JCMT/POL2 magnetic field measurement rendition share the same scaling relation with the FIREPLACE scale according to their polarization fraction. For visual clarity, we display all 850 μm magnetic field detections with polarization fraction exceeding $p = 0.08$ with a length equivalent to an 8% polarized pseudovector.

polarization fraction tends to be relatively higher in low-intensity regions and lower in high-intensity regions. This can either be due to the loss of grain alignment in denser regions or due to the presence of multiple independent domains of different magnetic field orientations along the line of sight in the high-column density regions, therefore decreasing the integrated polarization fraction in high-column-density (and thus high-intensity) regions. The faint regions, typically present in the periphery of molecular clouds, appear more uniform in magnetic field orientation. The region where this anticorrelation is most obvious is the head-tail cloud, extending from the G359.44-0.10 extended green object (EGO), where both 214 and 850 μm magnetic field detections exhibit extremely low polarization fractions, while the intensity is high at both of these wavelengths.

In particular, we observe an elongated far-IR-dark region along $\boldsymbol{b = -0.^{\circ}08}$ in Figure 3. This region corresponds to the Galactic plane and is home to many compact mid-IR sources and short and curved radio filamentary structures (H. S. Liszt & R. W. Spiker 1995; S. J. Carey et al. 2009; F. Yusef-Zadeh et al. 2009; M. J. Hankins et al. 2020; A. S. Cotera et al. 2024). The low 214 μm intensity and polarization nondetections there indicate a relative absence of cold dust, where it has either been heated by the local radiation field, expelled by stellar winds and expanding H II regions, or there is simply a dearth of material there.

3.2. DCF Analysis

We adopt a modified Davis–Chandrasekhar–Fermi (DCF) method (L. Davis 1951; S. Chandrasekhar & E. Fermi 1953) to

calculate the sky-plane magnetic field strength using the polarization measurements from FIREPLACE III. The sky-plane magnetic field strength, following the DCF method, is expressed as

$$|\boldsymbol{B}_{\rm POS}| = \sqrt{4\pi\rho_m}\frac{\sigma_v}{\sigma_\phi}, \tag{2}$$

where ρ_m is the mass density, σ_v is the velocity dispersion of the gas content, and σ_ϕ is the angular dispersion of the magnetic field pseudovectors. The DCF method is based on the assumption that the energy density of the turbulent or random gas motions is equal to the energy density of the fluctuations of the magnetic field about the local mean field, where its velocity dispersion is assumed to be isotropic. Although the general principle of the DCF method is commonly agreed upon, specific measurements of the input parameters of Equation (2) are under active refinement and debate, especially in the context of a dynamically complex region like the GC (J. A. Guerra et al. 2023; N. O. Butterfield et al. 2024b; X. Lu et al. 2024). In our DCF analysis, we do not consider the effect of shear on the sky-plane magnetic field strength $|\boldsymbol{B}_{\rm POS}|$ (e.g., the shear-flow approximation considered by J. A. Guerra et al. 2023). Therefore, there is a caveat that our analysis can overestimate $|\boldsymbol{B}_{\rm POS}|$ as the shear could lower the angular dispersion. However, due to the highly turbulent nature of the Sgr C region, shear does not play a significant role in the estimated magnetic field strength, as it is only significant in clouds with uniform motion. We address our methodology for estimating the inputs ρ_m, σ_v, and σ_ϕ to calculate the magnetic field strength $|\boldsymbol{B}_{\rm POS}|$ as in Equation (2) in the following subsections.

3.2.1. Angular Dispersion (σ_ϕ)

Past decades of research have shown that the GC magnetic field exhibits different behaviors viewed from different observational scales: a pervasive and ordered magnetic field in large scale (G. Novak et al. 2003; Planck Collaboration et al. 2015; A. Mangilli et al. 2019; Y. Guan et al. 2021), a turbulent magnetic field driven by local environments in molecular clouds in small scale (D. T. Chuss et al. 2003; N. O. Butterfield et al. 2024b; FIREPLACE I; X. Lu et al. 2024; FIREPLACE IV), and a vertical intercloud field signified by the NTFs (E. Serabyn & M. Morris 1994). However, in a dynamically complex region like the CMZ, the relative contribution of magnetic field systems on different scales is still under investigation. To this end, we follow the methods developed by R. H. Hildebrand et al. (2009) and M. Houde et al. (2009), which have been implemented in numerous SOFIA/HAWC+ studies (D. T. Chuss et al. 2019; J. A. Guerra et al. 2021; N. O. Butterfield et al. 2024b; FIREPLACE I). We direct interested readers to M. Houde et al. (2009, 2016) for a detailed account of this method. The analysis in this subsection was implemented using the POLBPY software (J. A. Guerra et al. 2024).

We now detail the specific procedure, which separately accounts for the sky-plane magnetic field contribution from large and small scales. We write the sky-plane magnetic field as a superposition $\boldsymbol{B}_{\rm POS} = \boldsymbol{B}_0 + \boldsymbol{B}_t$, where $\boldsymbol{B}_0$ is the ordered, large-scale field, and $\boldsymbol{B}_t$ is the turbulent, small-scale field. The angular dispersion can then be approximated as the turbulent-to-ordered magnetic field energy ratio (M. Houde et al. 2009):

$$\sigma_\phi^2 \approx \frac{\langle \boldsymbol{B}_t^2\rangle}{\langle \boldsymbol{B}_0^2\rangle}. \tag{3}$$

To determine this ratio, we adopt a two-component structure function, again separately accounting for the large- and small-scale magnetic field systems. As a statistical measure of the polarization angle difference $\Delta\phi(l) \equiv \phi(\boldsymbol{r}+\boldsymbol{l}) - \phi(\boldsymbol{r})$ at a distance scale l, the structure function $1 - \langle\cos[\Delta\phi(l)]\rangle$ can be computed using our polarization measurements. As such, fitting our two-component function to the empirical results (i.e., the FIREPLACE measurements) can constrain the contribution to the overall magnetic field strength from both scales, thereby yielding the required turbulent-to-ordered field ratio to calculate angular dispersion using Equation (3).

The two-component structure function is written as (M. Houde et al. 2009)

$$1 - \langle\cos[\Delta\phi(l)]\rangle = \frac{1 - e^{-l^2/2(\delta^2+2W^2)}}{1 + \mathcal{N}\left[\frac{\langle \boldsymbol{B}_t^2\rangle}{\langle \boldsymbol{B}_0^2\rangle}\right]^{-1}} + a_2 l^2, \tag{4}$$

where δ is the correlation length for the turbulent field, W is the beam radius, and a_2 is the large-scale contribution coefficient. Moreover, $\mathcal{N}$ is the number of turbulent cells along the line of sight defined by M. Houde et al. (2009) as

$$\mathcal{N} = \frac{(\delta^2 + 2W^2)\Delta'}{\sqrt{2\pi}\,\delta^3}, \tag{5}$$

computed for a given region, where Δ' is the cloud's effective depth. In Equation (4), the first term on the right-hand side describes small-scale turbulence, and the second describes the large-scale contribution.

Before fitting Equation (4), we follow M. Houde et al. (2009) and infer Δ' using the shape of the autocorrelation function

$$\langle \bar{P}^2(l)\rangle \equiv \langle \bar{P}(\boldsymbol{r})\bar{P}(\boldsymbol{r}+\boldsymbol{l})\rangle, \tag{6}$$

where $\bar{P}(\boldsymbol{r})$ is the beam-integrated polarized flux at the coordinate $\boldsymbol{r}$. Instead of using the default array-by-array approach taken by the POLBPY package, we use a fast Fourier transform to compute $\langle \bar{P}^2(l)\rangle$. Intuitively, Equation (6) is a statistical measure of the average polarized flux within a distance l in the sky-plane, thereby giving the approximate spatial extent of the part of a cloud having the bulk of a coherent magnetic field orientation in the sky-plane. Assuming the cloud is isotropic, we posit that the distribution of polarized flux along the cloud's depth is similar to its sky-plane projection. We thereby follow M. Houde et al. (2009) and use the half-width at half-maximum (HWHM) value as the effective cloud depth. However, because the Sgr C complex consists of several regions identifiable by their spatial and radial velocity separation, or by the overall trends in their magnetic field orientations, the dispersion calculation only remains meaningful if applied to individual regions with their own identifiable magnetic field system. Therefore, we visually group the Sgr C magnetic fields based on their large-scale trends and only conduct DCF analyses using the magnetic field pseudovectors within a given region. The regions that we have thereby identified, along with their spatial extents, are shown

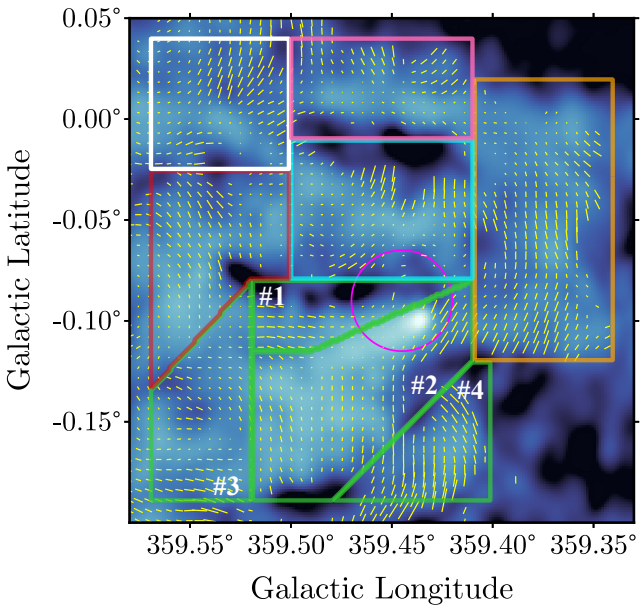


Figure 4. Individual regions used in the DCF analysis when fitting Equation (4), overlaid with the 214 μm intensity image and pseudovector representation. The magenta circle marks the extent of the Sgr C H II region. We note that the -65 km s^{-1} cloud is separated into four numbered regions (number-labeled green polygons).

in Figure 4. We list their computed effective cloud depths computed from Equation (6) in Table 1. The individual clouds in Sgr C have a typical effective cloud depth of $\tilde{1}'$ or 2.38 pc. However, given the known line-of-sight overlap of clouds in Sgr C (C. C. Lang et al. 2010), the composite depths of this region could be much larger than interpreted on the level of individual clouds. More details regarding the autocorrelation function and effective cloud depth of each region can be found in Appendix.

Having estimated the effective cloud depth, we perform a Markov Chain Monte Carlo (MCMC) fit of Equation (4) for variables δ, a_2, and, most importantly, $\langle \boldsymbol{B}_t^2 \rangle / \langle \boldsymbol{B}_0^2 \rangle$ for all pixels in the field of view. The POLBPY package uses the EMCEE package (D. Foreman-Mackey et al. 2013) to generate MCMC posterior distributions of parameters δ and a_2, but does so for $\langle \boldsymbol{B}_t^2 \rangle / \langle \boldsymbol{B}_0^2 \rangle$ through a similar quantity $\Delta'(\langle \boldsymbol{B}_t^2 \rangle / \langle \boldsymbol{B}_0^2 \rangle)^{-1}$. All parameters are constrained to be positive with no upper bounds, although we do note that δ cannot be greater than the diameter of the dispersion function's circular kernel. The fit was performed on the structure function with $l \leqslant 1.'25$ to ensure that only local dispersion is sampled. Here, we note that the behavior of the kernel on the boundaries between regions can lead to improperly defined dispersion functions and therefore less-then-optimal fitted parameters. However, the MCMC fitting routine solves for the quantity $\Delta'(\langle \boldsymbol{B}_t^2 \rangle / \langle \boldsymbol{B}_0^2 \rangle)^{-1}$ for each pixel, which allows for using a pixel-dependent value of effective depth (see J. A. Guerra et al. 2021). Furthermore, to improve the efficiency of the MCMC fits, we calculate and fit the dispersion functions using all available polarization measurements within one region shown in Figure 4. The best-fit results are then used as the initial condition of the pixel-by-pixel MCMC fit to accelerate convergence. The final results were obtained with 300 iterations for each pixel, at which point we manually inspected the MCMC fit at numerous locations to ensure convergence. We found that the fit results do not evolve significantly after 150 iterations. The resulting images of the variables are shown in Figure 5.

Table 1
The Effective Cloud Depths for Individual Regions Shown in Figure 4

Cloud	Color/Number	Δ' (arcmin)	Δ' (pc)
-65 km s^{-1} cloud #1	Green #1	0.64 ± 0.15	1.45 ± 0.36
-65 km s^{-1} cloud #2	Green #2	1.43 ± 0.20	3.24 ± 0.36
-65 km s^{-1} cloud #3	Green #3	1.03 ± 0.08	2.45 ± 0.19
-65 km s^{-1} cloud #4	Green #4	1.04 ± 0.13	2.48 ± 0.31
FIR-4	Pink	0.84 ± 0.13	2.00 ± 0.31
Galactic plane	Red	1.39 ± 0.22	3.32 ± 0.52
Source C	Orange	1.41 ± 0.14	3.36 ± 0.33
Far Northeast	White	1.36 ± 0.07	3.24 ± 0.17
-90 km s^{-1} cloud	Cyan	1.09 ± 0.12	2.60 ± 0.29

Globally, the a_2 and $\langle \boldsymbol{B}_t^2 \rangle / \langle \boldsymbol{B}_0^2 \rangle$ values are positively correlated, and they are negatively correlated with δ. Given the high column density in many clouds in Sgr C, an increase in turbulence (which entails a decrease in turbulent correlation length) likely decreases the polarization fraction integrated along a line of sight. Therefore, the large-scale contribution $\boldsymbol{B}_0$ naturally becomes the dominant term relative to the turbulent contribution $\boldsymbol{B}_t$ in highly turbulent regions. We also note that, given the issue of moving the kernel near regional boundaries, the $\langle \boldsymbol{B}_t^2 \rangle / \langle \boldsymbol{B}_0^2 \rangle$ results on the boundaries should be taken with caution. The observed discontinuities in Figure 5 are more likely due to an unresolved δ parameter in some regions, which is a consequence of limited angular resolution.

Among the three high-density molecular clouds, we note that FIR-4 and the -90 km s^{-1} cloud exhibit more diverging magnetic field directions than the -65 km s^{-1} cloud, as can be observed in the cyan and pink regions in Figure 4. In particular, the region immediately north of the Sgr C H II region has a high turbulent-to-ordered ratio, which is likely induced by the compression from the ongoing expansion of the H II region. On the contrary, the relatively uniform -65 km s^{-1} cloud and the source C cloud do not exhibit a significant spatial variation for these parameters, except for the area of the head-tail feature, where the polarization fraction is extremely low (see Figure 3).

3.2.2. Mass Density (ρ_m)

We infer the mass density by deriving a column density image using the Hi-GAL survey data (S. Molinari et al. 2010, 2016). Our procedure largely follows the spectral energy distribution (SED) fitting process described in Section 3.1.3 of D. T. Chuss et al. (2019) and Section 2.2 of FIREPLACE IV. Our SED fitting includes the Hi-GAL survey images from 160, 250, and 350 μm. We did not include the 70 μm image due to its uncertain extinction correction (M. Compiègne et al. 2010; C. Battersby et al. 2011, 2025). The 500 μm image was also excluded due to its low resolution. The images are convolved with a Gaussian kernel to match the 24″ resolution of the SPIRE 350 μm image. Following the convolution, we perform a pixel-by-pixel SED fitting to the single-temperature modified blackbody modeled by J. E. Vaillancourt (2002)

$$I_\nu(\nu, T) = (1 - e^{-\tau(\nu)}) B_\nu(T), \quad (7)$$

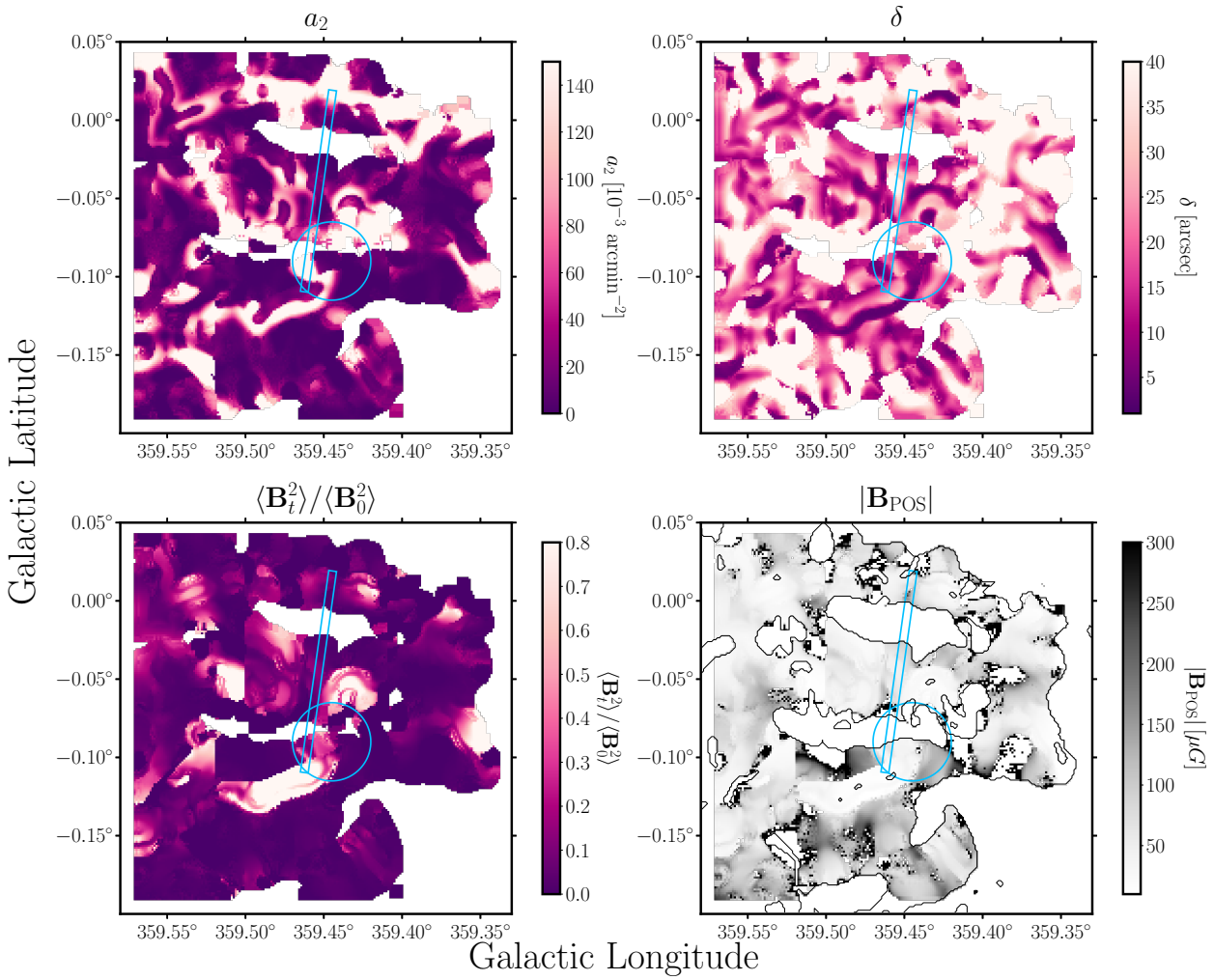


Figure 5. Images of the best-fit structure function variables a_2 (top left), δ (top right), $\langle \boldsymbol{B}_t^2 \rangle / \langle \boldsymbol{B}_0^2 \rangle$ (lower left), and the sky-plane magnetic field strength $|\boldsymbol{B}_{\rm POS}|$ (lower right) in Sgr C. The blue circle and rectangle denote the approximate location of the Sgr C H II region and NTF, respectively. We make a 2σ cut for the fitting variables prior to displaying these images. A small number of pixels with $|\boldsymbol{B}_{\rm POS}| > 10$ mG was manually removed to eliminate unphysical field strength.

where B_ν is the Planck function. The optical depth $\tau(\nu)$ is defined as

$$\tau(\nu) = \epsilon \left(\frac{\nu}{\nu_0} \right)^\beta, \tag{8}$$

where ϵ is a constant proportional to the column density, and ν_0 is the frequency normalization constant adopted from S. I. Sadavoy et al. (2013). For the fit, we leave ϵ and T as free parameters while fixing $\beta = 2$. Finally, the column density at each pixel is computed as

$$N(\mathrm{H_2}) = \frac{\epsilon}{\kappa_{\nu_0} \mu m_{\rm H}}, \tag{9}$$

where κ_{ν_0} is the reference dust opacity, μ is the mean molecular weight per hydrogen atom, and $m_{\rm H}$ is the atomic mass of hydrogen. We adopt $\nu_0 = 1000$ GHz, $\kappa_{\nu_0}(1000\ \mathrm{GHz}) = 0.1\ \mathrm{cm^2\ g^{-1}}$, and $\mu = 2.8$ as the mean molecular weight of hydrogen. The derived column density map is shown in Figure 6.

As expected, the cold molecular clouds, such as FIR-4, the $-65\ \mathrm{km\ s^{-1}}$ cloud, and the $-90\ \mathrm{km\ s^{-1}}$ cloud, which dominate the far-IR emission, are the most prominent in this map. We compare our column density result with that of C. Battersby et al. (2025), which uses a slightly different method and also excludes the 70 μm image, as well as FIREPLACE IV, which used the same method as this work but includes the 70 μm Hi-GAL image. The column density values are similar across these works upon comparison. The mass density is then calculated in each region as

$$\rho_m = \mu m_H \frac{N(\mathrm{H_2})}{\Delta'}, \tag{10}$$

following J. A. Guerra et al. (2024).

3.2.3. Velocity Dispersion (σ_v)

Due to the highly turbulent nature of the clouds surrounding Sgr C, the velocity dispersion is quite large, as in most of the CMZ. We measure the velocity dispersion by taking the square root of the second spectral moment map of the HCN spectral cube provided by P. A. Jones et al. (2012) using the Common Astronomy Software Applications (CASA; CASA Team et al. 2022) package. Over the entire region, the velocity dispersion varies by only about 20% around a mean value of $10\ \mathrm{km\ s^{-1}}$, and the mean value within each of our defined regions varies by even less. Meanwhile, there are many instrumental artifacts contained in the velocity dispersion map calculated from

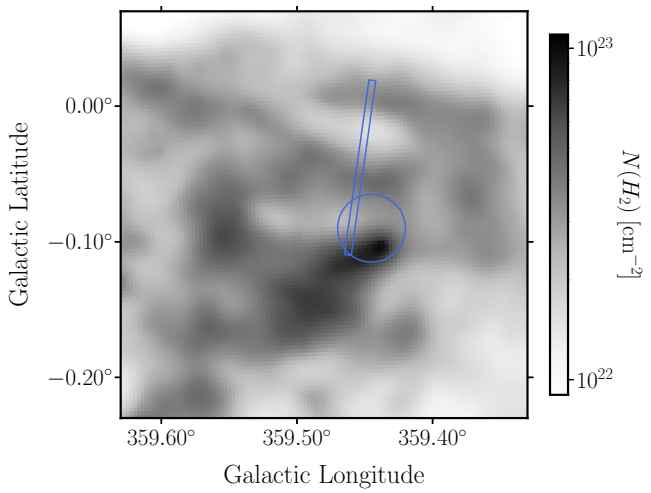


Figure 6. The column density map derived from fitting Equation (7) to the Hi-GAL 160, 250, and 350 μm images, displayed in a logarithmic scale. The blue circle and rectangle indicate the locations of the Sgr C H II region and the Sgr C NTF, respectively.

Mopra spectral cube, which cannot be easily mitigated. Given the inherent uncertainty in our sky-plane magnetic field strength determinations owing to the fact that we only have access to the intensity-weighted average of the velocity dispersion along the line of sight, and similarly for the magnetic field orientations, we have chosen to adopt a constant velocity dispersion of 10 km s^{-1}. The resulting field strength estimates vary linearly with the adopted velocity dispersion (see Equation (2)).

3.2.4. Magnetic Field Strength Results

The sky-plane component of the magnetic field strength calculated from the above-described inputs using Equation (4) is displayed in the lower right panel of Figure 5. The field strength exhibits a large range from ∼30 μG to ∼400 μG. This range agrees with many past attempts to infer the CMZ magnetic field strength (D. T. Chuss et al. 2003; R. M. Crocker et al. 2010; J. M. D. Kruijssen et al. 2014; M. C. Sormani et al. 2020; R. G. Tress et al. 2024). We find that the morphology of the angular or velocity dispersion image has a limited effect on the inferred $|\boldsymbol{B}_{\rm POS}|$, but the local turbulence of a region is anticorrelated with $|\boldsymbol{B}_{\rm POS}|$ (shown in the bottom panels of Figure 5). Therefore, the dominant factor affecting $|\boldsymbol{B}_{\rm POS}|$ is the local shear and compression. On the scale of individual molecular clouds, this conclusion suggests that the most turbulent clouds (FIR-4, the −90 km s^{-1} cloud, and the −65 km s^{-1} cloud) exhibit the lowest $|\boldsymbol{B}_{\rm POS}| \sim 100$ μG.

The head-tail cloud (which extends from the southern portion of the Sgr C H II region, see Figure 2) displays intriguing features from our DCF analysis. The low polarization fraction "tail" detected in both 214 and 850 μm surveys extending from the G359.45-0.10 "head" displays a consistently lower $|\boldsymbol{B}_{\rm POS}|$, creating a sharp contrast with the high field strength regions in clouds with uniform field direction. Once more, the low $|\boldsymbol{B}_{\rm POS}|$ in the head-tail cloud likely signifies its high turbulence and complex composition (i.e., several clouds likely superposed along the same line of sight due to the high column density and low polarization fraction detected in both 214 and 850 μm).

We also highlight the morphology of the field near the Sgr C H II region. In the north of the H II region around $l = 359.^{\circ}43$, $b = -0.^{\circ}07$, a half-shell of low field strength is apparent. Simultaneously as a high turbulent-to-ordered ratio region, we speculate that the ionization front of the H II region may be the reason behind the high turbulence. Although the molecular cloud there has a high column density, the turbulence induced by the shock and ionization front driving the expansion presumably leads to an overall low $|\boldsymbol{B}_{\rm POS}|$.

We note a few caveats in our DCF analysis. One should be cautious that the FIREPLACE survey is conducted in a single wavelength. The 214 μm filter tends to sample clouds with colder temperatures (colder compared to the warmer Sgr C H II region; S. J. Carey et al. 2009, M. J. Hankins et al. 2020), which in some regions may only be one of multiple clouds along the line of sight. The most obvious example in Sgr C is a cloud centered at $l = 359.^{\circ}48$, $b = -0.^{\circ}17$ with a broad range of velocities (from −92.6 to −34.3 km s^{-1}) detected in the HCN line analysis presented in Section 4.2. The 850 μm measurements from X. Lu et al. (2024) nicely trace the morphology of this cloud but disagree with the 214 μm magnetic field orientations in this region, which may indicate that the 850 μm measurements are sampling a different cloud along that line of sight, which may naturally possess a different magnetic field orientation. As such, inferring $|\boldsymbol{B}_{\rm POS}|$ using only one wavelength introduces some uncertainty, since different clouds, or even the same cloud with different temperature domains, along a given line of sight can have independent field directions that then lead to a reduction of the polarization fraction. Another possible source of error comes from the column density estimation. As we assume a single-temperature blackbody, having multiple clouds (possibly with different temperatures) along the same line of sight could cause an error in our column density estimation, which also affects the $|\boldsymbol{B}_{\rm POS}|$ calculation. In regions dominated by higher temperatures, the DCF analysis cannot be reliably performed since there is an absence of valid 214 μm magnetic field detections.

4. Multiwavelength Observations

This section provides an overview of the relevant features of Sgr C by comparing existing multiwavelength studies with the FIREPLACE 214 μm magnetic field measurements.

4.1. Assembly of Observations

Figure 7 shows nine intensity images covering a broad range of wavelengths, from 1 nm to 20 cm, to highlight the significant structures in the Sgr C region. Of the published surveys of the Sgr C region, the images presented in Figure 7 have been chosen to avoid repetition. For example, the 870 μm APEX/ATLASGAL survey (F. Schuller et al. 2009) is not included because it exhibits features nearly identical to those in the JCMT/SCUBA 850 μm survey (D. Pierce-Price et al. 2000).

The Galactic plane appears bright in the IR regime out to 70 μm and in radio, with the peak emission at these wavelengths arising near the Sgr C H II region. In mid-IR and radio images (panels (2)–(4), and (7) in Figure 7), the Sgr C H II region exhibits a similar elliptical morphology elongated along the Galactic plane. We observe an absorption "tail" originating from inside the Sgr C H II region extending toward the southeast, where the EGO is located (G359.44-0.10;

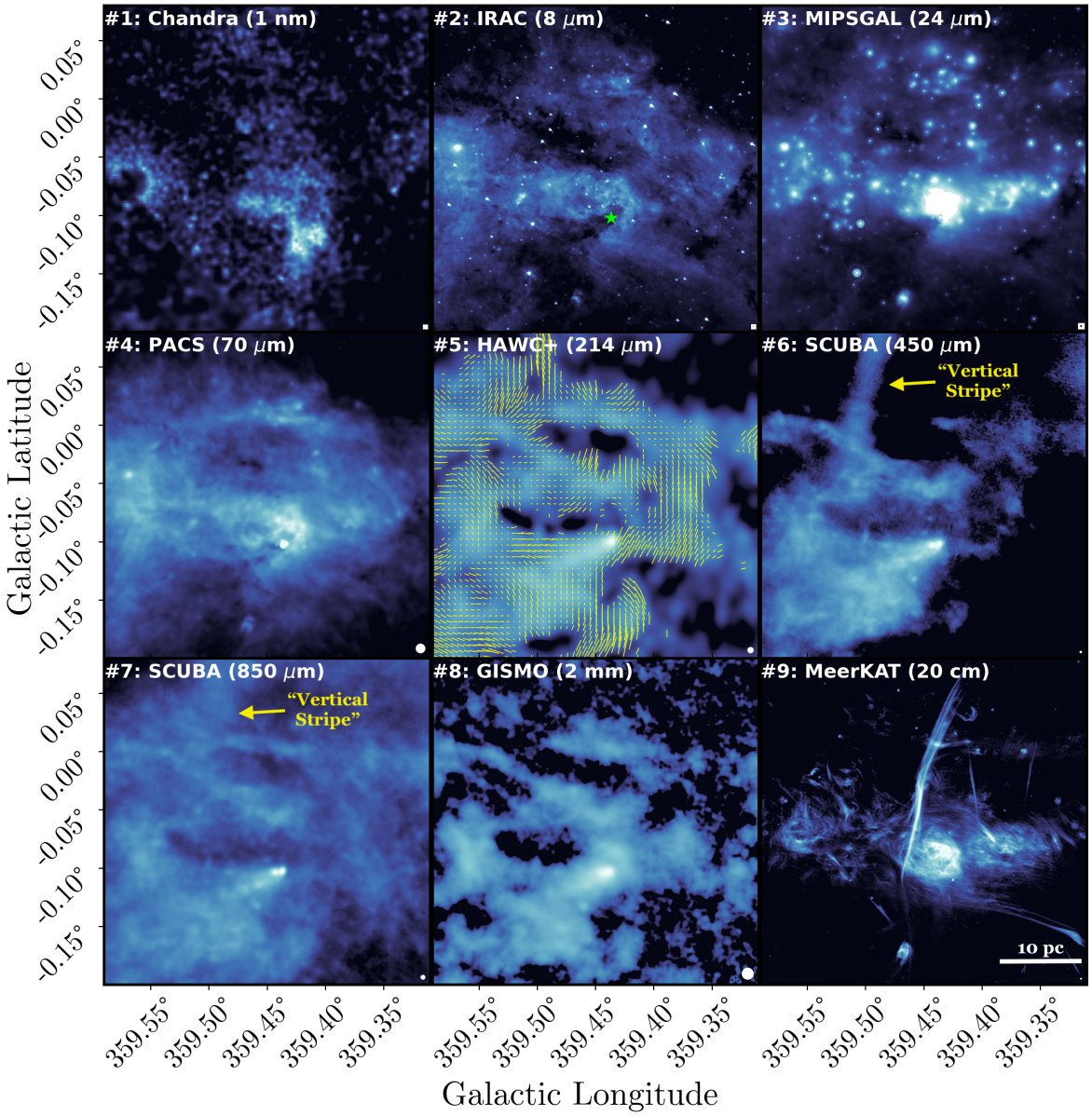


Figure 7. Selected multiwavelength images of the Sgr C complex. The region has been surveyed in 1–4 keV X-rays by Chandra (Q. D. Wang 2021), 8 μm by Spitzer/IRAC (S. Stolovy et al. 2006), 24 μm by Spitzer/MIPSGAL (S. J. Carey et al. 2009), 70 μm by Herschel/PACS (S. Molinari et al. 2010), 214 μm by SOFIA/HAWC+ (D. Paré et al. 2024), 450 and 850 μm by JCMT/SCUBA (D. Pierce-Price et al. 2000), 2 mm by IRAM/GISMO (R. G. Arendt et al. 2019), and at 20 cm by MeerKAT (I. Heywood et al. 2022). For visual comparison between the multiwavelength images and the magnetic field detections, we add the 214 μm magnetic field pseudovectors from D. Paré et al. (2024) in panel (5) as yellow segments. The corresponding beam sizes are displayed as white circles in the lower right corner of each image. The green star in panel (2) labels the G359.44-0.10 EGO, and the yellow arrows in panels (6) and (7) indicates the location of a vertical structure in these maps. All images are displayed with a logarithmic stretch.

S. Kendrew et al. 2013; X. Lu et al. 2019, 2021; S. Crowe et al. 2024; labeled in panel (2) of Figure 7). This low-intensity "valley" is manifested at 8, 24, and 70 μm and is a result of foreground absorption by the head-tail cloud, which turns to emission at far-IR wavelengths beyond 70 μm. The mid-IR intensity images tend to become more diffuse at longer wavelengths, which is partially due to the trend that lower-temperature dust is generally the most extended, and partially due to decreased resolution at longer wavelengths.

The 8 μm emission traces the polycyclic aromatic hydrocarbons (PAHs) ionized by stellar UV radiation (S. Stolovy et al. 2006; D. Narayanan et al. 2023), thereby showing the extent of the elliptical region impacted by UV emission and star formation around the Sgr C H II region. In the 8–70 μm interval (panels (2)–(4) in Figure 7), the emission also traces warm dust heated by stellar emission. In this band, one could also observe the "head" of the head-tail structure as an extremely compact and luminous source (classified as an EGO by S. Kendrew et al. 2013) to the immediate south of the H II region, also becoming more diffuse toward longer wavelengths.

In the far-IR regime (214–850 μm, panels (5)–(7) in Figure 7), the images are dominated by thermal emission from cold dust residing in molecular clouds. The Galactic plane and the H II region, by contrast, appear dark in the far-IR regime. The "head" of the head-tail structure is larger in size at

far-IR wavelengths than in the mid-IR. Although this increase in size could be a result of cold dust being more diffuse, it can again be a result of lower spatial resolution at far-IR wavelengths. The "tail" also appears bright at these wavelengths, reflecting a relatively high column density of cold dust. Indeed, we have an inferred column density of $\sim 10^{23}$ cm^{-2} in this region, shown in Figure 6.

A noteworthy structure is the vertical "stripe" extending northwards from $l = 359.^{\circ}52$, $b = -0.^{\circ}05$ that appears in the 450 and 850 μm SCUBA images (labeled by orange arrows in panels (6)–(7) in Figure 7), although it is most noticeable at 450 μm and is much more diffuse at 850 μm. With the caveat that this could be an artifact due to filtering, we note that the northern end of this "stripe" coincides with the mid-IR ridge that connects the extended thermal source AFGL5376 and the Galactic plane (K. Uchida et al. 1990; K. I. Uchida et al. 1994). The 214 μm magnetic field orientations do not bear any obvious relationship to the morphology of this stripe. We go no further than noting the above correspondence, as a discussion of AFGL5376 is beyond the scope of this paper.

As a transition between far-IR and radio wavelengths, the GISMO image at 2 mm displays characteristics from both regimes, showing a combination of thermal emission from cold dust and free–free synchrotron emission from ionized gas. As such, we see not only the 100 pc ring dominated by cold dust but also the ionized gas in the Sgr C H II region.

The radio continuum emission (panel (9) in Figure 7) is produced by free–free emission, primarily from the Sgr C H II region, and by synchrotron emission from the nearby NTFs (I. Heywood et al. 2022; F. Yusef-Zadeh et al. 2022b, 2022c), the most prominent of which is the Sgr C NTF bundle that appears to originate near the Sgr C H II region. Although the peak emission from the Sgr C NTF is at $b \gtrsim -0.^{\circ}10$ and is most obviously seen to extend toward the north, there is a faint extension toward the south, which ends near the relatively compact elliptical or bipolar radio source G359.46-0.17. We hypothesize that the abrupt intensity change in the NTF is caused by its interaction at that point with the high-density gas in the head-tail structure (detailed in Section 5.1.1). At that location, the diffusion of relativistic electrons to the south along the field lines is largely, but apparently not entirely, blocked by the presence of the dense gas. Furthermore, if the interaction with the cloud is taking place along the ionization front of the Sgr C H II region, the acceleration of the electrons to relativistic energies could be the result of magnetic field line reconnection there, as proposed by E. Serabyn & M. Morris (1994) or by diffusive shock acceleration if a strong stellar wind creates a shock front there (R. Rosner & G. Bodo 1996).

There are also abundant short and curved radio filamentary structures to the east of the Sgr C H II region along the Galactic plane, as noted in H. S. Liszt & R. W. Spiker (1995). Some of these radio structures can be nonthermal, as inferred by the absence of IR counterparts. Their relative faintness could simply be interpreted in terms of a smaller population of relativistic electrons. We also do not observe any correspondence between the FIREPLACE magnetic field orientations and these short radio filaments.

4.2. Spectral Line Analyses

To better understand the dynamics of Sgr C, we require the relative position and motion of the observed structures. Here, we appeal to the 3 mm Mopra spectroscopic survey conducted by P. A. Jones et al. (2012) and the H I absorption analysis by C. C. Lang et al. (2010) for velocity constraints and line-of-sight placements.

4.2.1. Structure of Clouds in Sgr C

We select the HCN $J = 1$–0 line to deduce the dynamical structure of the clouds in Sgr C to aid our understanding of the FIREPLACE magnetic field orientations. The HCN $J = 1$–0 line is one of the most prominent lines in the GC, arising in relatively dense gas (P. A. Jones et al. 2012). Figure 8 shows the velocity channel maps of this line in the velocity range from -92.6 to -34.3 km s^{-1}. We note that a foreground cloud often referred to as the "3 kpc arm" causes significant absorption around -50 km s^{-1} (C. C. Lang et al. 2010). The channel maps in Figure 8 show a coherently decreasing radial velocity from the north of the Sgr C H II region ($\gtrsim -90$ km s^{-1}, which is constituted of FIR-4 and the -90 km s^{-1} cloud) to the southeast (~ -65 km s^{-1}, which is constituted of the head-tail cloud and the -65 km s^{-1} cloud). These velocities follow the 100 pc dust ring revealed by S. Molinari et al. (2011). The radial velocity of FIR-4 (G359.45+0.02) is similar to that of the nearby -90 km s^{-1} cloud, which is a part of the 100 pc ring. FIR-4 is therefore likely physically related to the 100 pc ring.

The Sgr C H II region is largely devoid of HCN emission, except for the intruding head-tail cloud. Both the radio recombination line measurements reported by H. S. Liszt & R. W. Spiker (1995) and H I absorption analysis by C. C. Lang et al. (2010) determined the velocity of the H II region to be ~ -60 km s^{-1}. Given the velocity structure observed in Figure 8, we infer that the -90 km s^{-1} cloud, the -65 km s^{-1} cloud, and the Sgr C H II region constitute a continuous structure linked to the 100 pc ring, and are likely intrinsically related. We direct the reader to more details of the line-of-sight placement of structures in Sgr C in Section 3.6.3 of C. C. Lang et al. (2010).

In the southern portion of the -65 km s^{-1} cloud, there is a bright bulk of HCN emission at $l = 359.^{\circ}47$, $b = -0.^{\circ}17$ visible at all displayed velocities. In this region, we do not find any morphological relationship between the HCN emission and the 214 μm magnetic field orientations. However, many 850 μm magnetic field detections were reported in this cloud by X. Lu et al. (2024), and they do not generally agree with the 214 μm results of FIREPLACE III. The HCN emission offers several possible explanations for this discrepancy. It could be that this is a particularly disturbed and turbulent cloud with multiple temperature components, or there could be multiple clouds superposed along the same line of sight, as we previously suggested in Section 3.2.4. Both can cause the magnetic field measured from different wavelengths to exhibit different orientations. It is also likely that this cloud has a radial velocity gradient along the line of sight, given that this is where the rotating 100 pc ring reverses the direction in the projection. The observation of this particularly broad-linewidth cloud reaffirms our caveat for the DCF analysis in Section 3.2.4 regarding the incomplete accounting for multiple line-of-sight clouds having different velocities in the derivation of the magnetic field strengths.

The previously mentioned 214 μm magnetic field measurement cavity at $l = 359.^{\circ}44$, $b = -0.^{\circ}13$ between the -65 km s^{-1} cloud and Cloud #4 (centered at $l = 359.^{\circ}43$, $b = -0.^{\circ}17$; see Figure 4) is of interest to be studied. In Figure 8, the

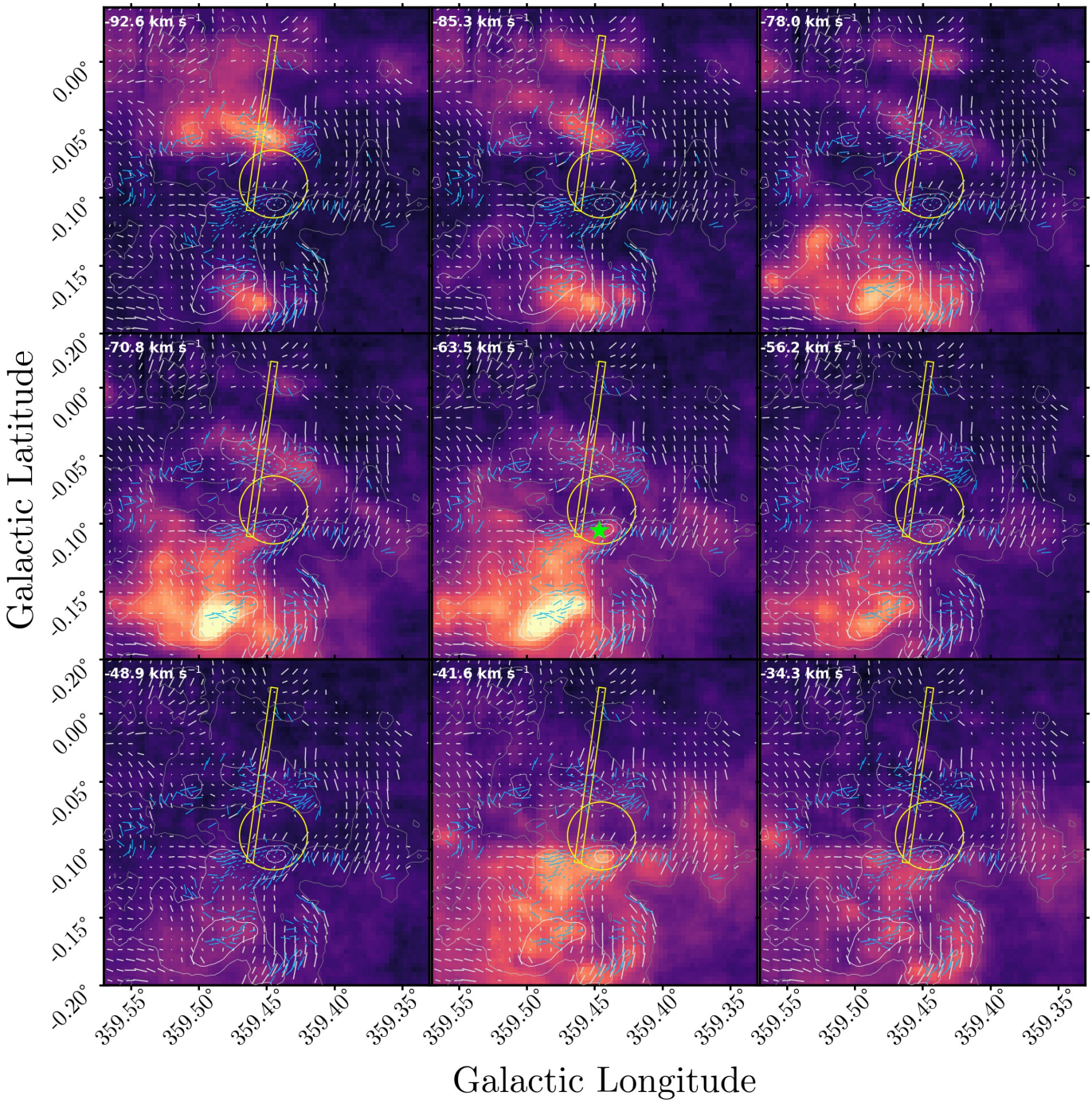


Figure 8. Velocity channel maps of the HCN $J = 1$–0 line measured by the 3 mm Mopra survey (P. A. Jones et al. 2012). The survey has spatial and spectral resolutions of 36″ and 1.84 km s^{-1}, respectively. The mean velocity of each channel is indicated in the top left corner. These channel maps cover the velocity range between −92.6 and −34.3 km s^{-1} in steps of 7.3 km s^{-1}. The gray-scale contours show the peak emission of HCN integrated through all observed velocities drawn at 0.75, 1.25, 1.75 K km s^{-1}, with the brighter contours indicating higher intensity. The white line segments are the 214 μm FIREPLACE magnetic field pseudovectors from D. Paré et al. (2024), and the blue segments are the 850 μm magnetic field pseudovectors from X. Lu et al. (2024). The yellow schematics indicate the approximate placement and extent of the Sgr C H II region and the Sgr C NTF. The green star in the central panel denotes the location of the G359.44-0.10 EGO, which is addressed in detail in Section 5.3. The global low intensity in channels near −50 km s^{-1} is due to absorption in the foreground "3 kpc arm" (C. C. Lang et al. 2010). The 214 μm magnetic field pseudovectors in this figure are rendered using Nyquist sampling at the Mopra beam size.

−65 km s^{-1} cloud and Cloud #4 appear to be portions of a continuous structure, so they are likely physically related. We hypothesize that they started as one cloud and were later separated into the currently observed shape by an outside force that created the magnetic field measurement cavity at $l = 359.^{\circ}44$, $b = -0.^{\circ}13$. We note a potentially relevant X-ray association with this cavity in Section 5.2.2.

4.2.2. Shock Tracer in the Twisted 100 pc Ring

As mentioned in the introduction, Sgr C is located on the western vertex of a dust ring (S. Molinari et al. 2011), and is postulated to be a collision site of X_1–X_2 orbits due to the bar potential (M. C. Sormani et al. 2018, 2020), which likely induces shocks and star formation. Meanwhile, the expanding

Sgr C H II region can also induce a compression front that collides with surrounding molecular clouds (H. S. Liszt & R. W. Spiker 1995) and add to the effect of the large-scale shocks. We employ the many 214 μm magnetic field detections toward the molecular clouds in the Sgr C region to examine how such shocks might be manifested in the magnetic field orientations. Figure 9 shows the velocity channel maps of the SiO $J = 2$–1 line, a known shock tracer also from the Mopra survey (P. A. Jones et al. 2012). The SiO channel maps exhibit a similar velocity structure to that of HCN, indicating that the SiO emissions are from within the 100 pc ring. However, the SiO emission appears much less spatially extended than that of HCN and more concentrated around the Sgr C H II region. This local enhancement of SiO indicates that the portions of the 100 pc ring surrounding the Sgr C H II region are particularly subjected to shocks, likely due to a combination of (1) the impact of the dust lane inflowing along the Galactic bar upon the CMZ material in the 100 pc ring, and (2) the collision between ambient gas and the expanding shell surrounding the H II region (D. Riquelme et al. 2025, in preparation). The collision likely increases the turbulence within the 100 pc ring, ultimately leading to a low polarization fraction, a higher turbulent-to-ordered magnetic field strength ratio, and relatively low inferred sky-plane magnetic field strength, as shown in Figure 5.

5. Individual Features in the Sgr C Complex

In this section, we use the 214 μm magnetic field measurements from FIREPLACE III along with multiwavelength images to draw inferences about individual features in the Sgr C complex.

5.1. Associated NTFs and Radio Features

NTFs are valuable probes of the large-scale magnetic field in the intercloud volume of the central few hundred parsecs of the Galaxy (E. Serabyn & M. Morris 1994; M. Morris 2006; T. Thomas et al. 2020). The following subsections examine the magnetic field behavior around the NTFs and radio structures observed in the Sgr C region, keeping in mind that the FIREPLACE detections primarily probe the magnetic field within clouds.

5.1.1. The Sgr C NTF

Figure 10 shows the FIREPLACE 214 μm magnetic field pseudovectors superimposed upon five selected images covering the Sgr C NTF. This extended NTF appears luminous and compact below $l = -0.^{\circ}02$, and it splits into two parallel filaments and becomes fainter and more diffuse above this latitude. This NTF overlaps on the sky-plane with three distinct magnetic field intervals:

(i) below $b = -0.^{\circ}10$, where the faint end of this NTF disappears in the head-tail cloud and the $-65\,\mathrm{km\,s^{-1}}$ cloud (detailed in Section 5.1.5);
(ii) $-0.^{\circ}08 \lesssim b \lesssim -0.^{\circ}02$, where the FIREPLACE magnetic field detections arise from the $-90\,\mathrm{km\,s^{-1}}$ cloud;
(iii) above $b = 0°$, where this NTF overlaps with a magnetic field system dominated by FIR-4 (detailed in Section 5.1.2).

Interval (ii) above is roughly the extent of Part A as defined in S. Roy (2003) and C. C. Lang et al. (2010; also labeled in the leftmost panel of Figure 10). We note additionally that the Sgr C NTF has a faint end toward the south, detailed in Section 5.1.5.

In the radio continuum below $l = -0.^{\circ}02$ (indicated by the upper dashed line in the leftmost panel of Figure 10), the NTF has the same width, but Part A is more luminous than Part B (the part of the Sgr C NTF below $l = -0.^{\circ}08$ labeled in Figure 10; S. Roy 2003). The radio spectral index analysis of F. Yusef-Zadeh et al. (2022b) indicates that Part A has an average spectral index of ~ -1.02, and Part B has an average spectral index of ~ -0.65. In Part A, the magnetic field orientation near the NTF roughly follows its direction. As our magnetic field measurements sample the field from relatively cold clouds, the direction of the FIREPLACE magnetic field in the $-90\,\mathrm{km\,s^{-1}}$ cloud (labeled in the fourth panel in Figure 10) is consistent with the orientation of the Sgr C NTF, as are the 850 μm measurements of X. Lu et al. (2024). Moreover, the DCF analysis from Figure 5 shows that there is a "tunnel" of low turbulent-to-ordered ratio and high $|B_{\mathrm{POS}}|$ along the Sgr C NTF. However, such an alignment ceases beyond $l > -0.^{\circ}02$ due to an absence of magnetic field detections outside the molecular cloud. Additionally, the NTF becomes much more diffuse after departing from the molecular cloud toward the north. Above $l = 0°$, the magnetic field orientation and the Sgr C NTF are no longer aligned, which could be attributed to strong far-IR emission from FIR-4 dominating the magnetic field detections in that region.

5.1.2. FIR-4: G359.43+0.02

At the northern portion of the Sgr C NTF where it splits into two filaments and begins to fade out toward the north, lies a short, linear radio feature oriented parallel to the Galactic plane along $b \approx 0.^{\circ}01$, labeled in the leftmost panel of Figure 10. It was originally found and denoted as FIR-4 by S. F. Odenwald & G. G. Fazio (1984) in the course of their far-IR survey of the GC. FIR-4 and its counterparts are displayed in Figure 10. The mid-IR counterpart of FIR-4 is the G359.43+0.02 young stellar object (YSO) cluster reported by F. Yusef-Zadeh et al. (2009) and prominently displayed in the central panel of Figure 10.

Given its moderately strong far-IR brightness, many significant 214 μm magnetic field detections were made in FIR-4. Overall, the magnetic field exhibits a divergent morphology with the magnetic field pointing in the radial direction away from the center of the source. The polarization fraction in the center and near the radio thread is mostly small, but increases toward the periphery. The $|\boldsymbol{B}_{\mathrm{POS}}|$ in the center is also lower than that in the periphery (see Figure 5). We hypothesize that this morphology likely traces the outflow driven by protostellar winds, which induce high turbulence within the cluster but a collective, ordered outflow on the periphery. In particular, the radio counterpart of FIR-4 coincides with the region along $l = 0.^{\circ}01$ with the lowest polarization fraction. The radio and mid-IR emission from FIR-4, arrayed as they are along the base of the embedded stellar cluster, suggest that UV emission from nearby YSOs has heated the local dust and has produced an ionization front, which appears linear in the projection.

FIR-4 intersects with the Sgr C NTF in the projection on the plane of the sky. C. C. Lang et al. (2010) suggested that FIR-4 could have the same line-of-sight placement as the Sgr C NTF. Examining the MeerKAT image in detail, we find that the radio luminosity at the intersection of the east–west ridge of FIR-4 with a few of the two westernmost subfilaments of the

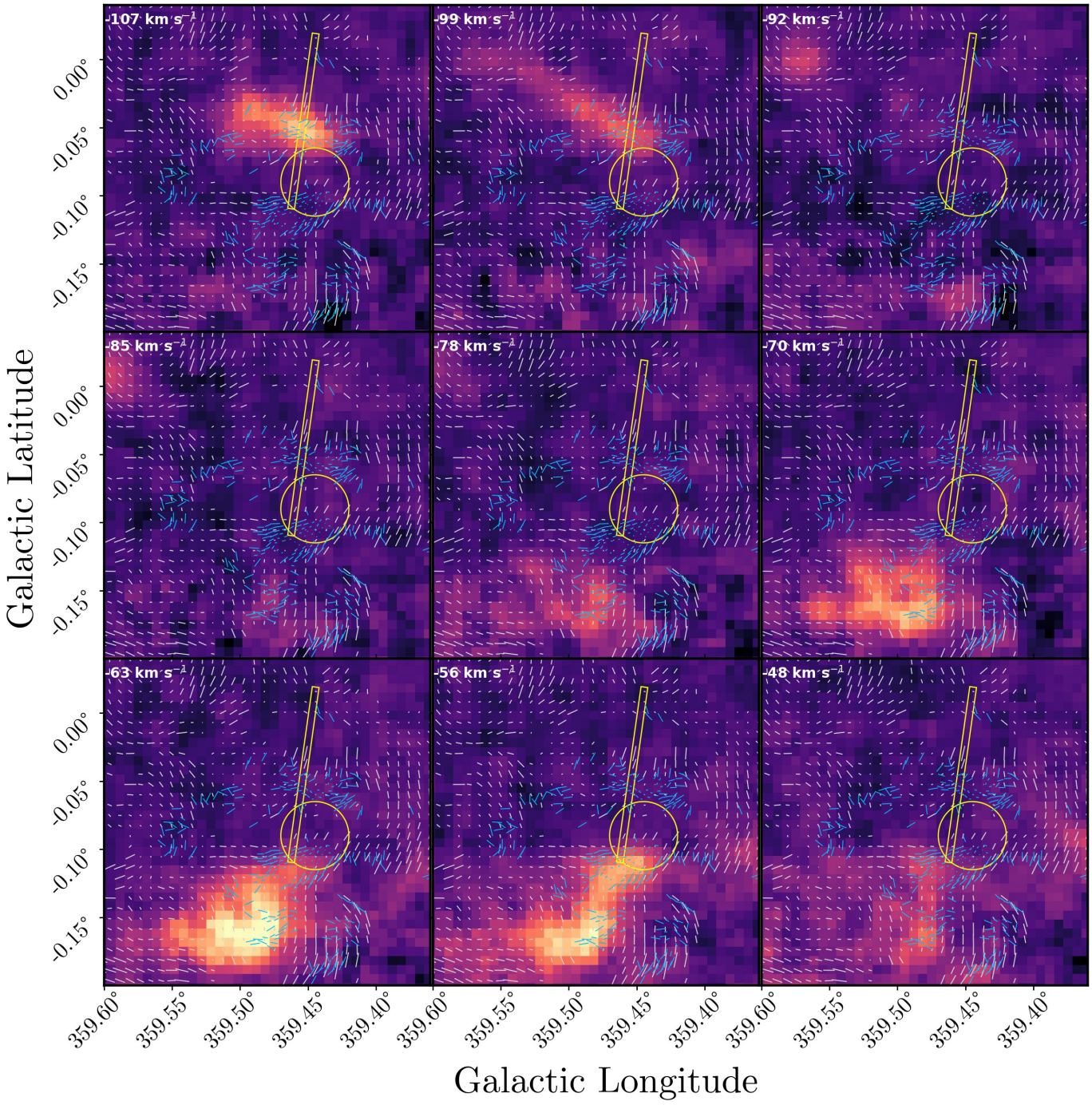


Figure 9. Velocity channel maps of SiO $J = 2$–1 emission between −110 and −49 km s^{-1}, measured by the Mopra survey (P. A. Jones et al. 2012). The 214 and 850 μm magnetic field pseudovectors are superimposed as white and blue line segments, as in Figure 8. The yellow schematic indicates the approximate location and extent of the Sgr C H II region and the Sgr C NTF.

NTF is ∼20% higher than the sum of individual luminosities of the neighboring regions of the superposed features. Moreover, the potential interaction site displays an increased north–south radio emission width (which is much larger than the MeerKAT beam size; seen in filament #13 in I. Heywood et al. 2022), and the NTF subfilaments brighten as they approach the intersection site from both the north and the south. These characteristics lead us to suggest that FIR-4 is interacting directly with the Sgr C NTF.

We note that there is an absence of magnetic field detections in the far-IR dark region that lies north of the Sgr C H II region at latitude $-0.^{\circ}02$ and south of the cluster of YSOs. This region has faint emission at both 8 and 24 μm, but gradually becomes negligible toward far-IR and radio frequencies (see Figure 10). This indicates that this region contains mainly diffuse warm gas, possibly heated by the nearby YSOs.

5.1.3. The G359.33-0.15 Filaments

A fainter bundle of parallel radio filaments, referred to as the "Hummingbird" by F. Yusef-Zadeh et al. (2022b), is located to the southwest of the Sgr C H II region. The northeastern end is

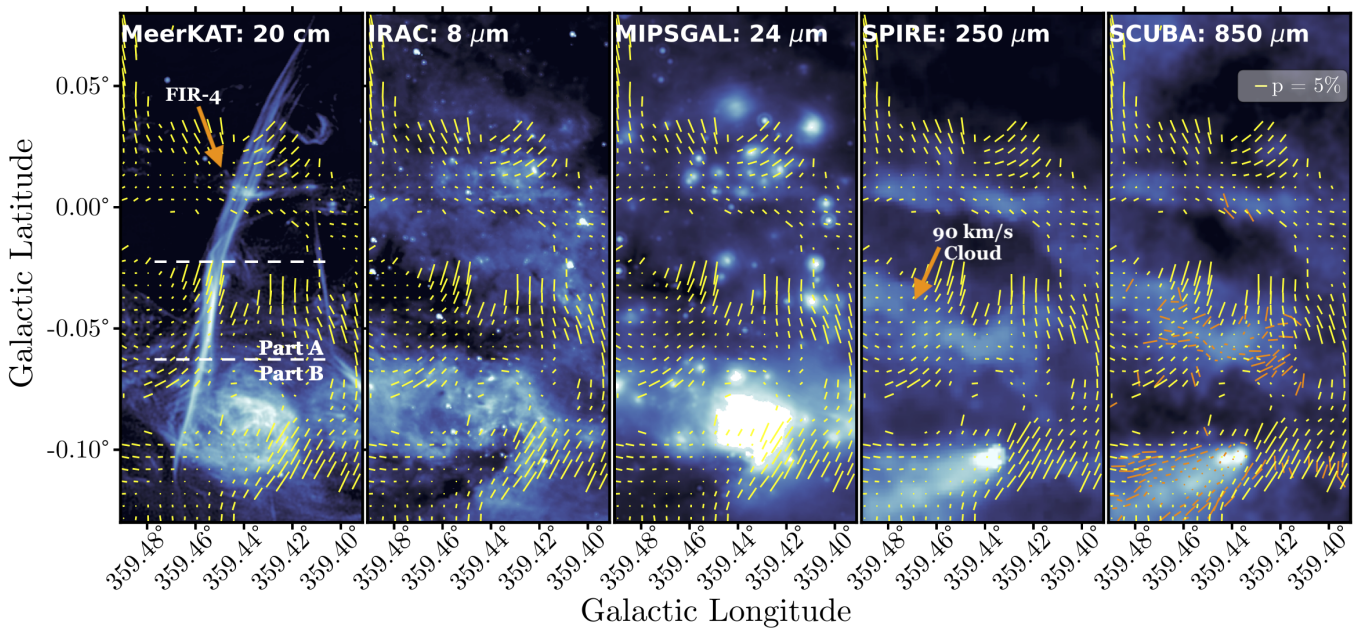


Figure 10. The 214 μm magnetic field pseudovectors near the Sgr C NTF and G359.43+0.02 YSO superimposed on emission at 20 cm (I. Heywood et al. 2022), 8 μm (S. Stolovy et al. 2006), 24 μm (S. J. Carey et al. 2009), 250 μm (S. Molinari et al. 2010), and 850 μm (D. Pierce-Price et al. 2000). The yellow segments are the 214 μm magnetic field pseudovectors from D. Paré et al. (2024), and the orange segments are the 850 μm magnetic field pseudovectors from X. Lu et al. (2024). Important features in this region, such as FIR-4, the two parts of the Sgr C NTF, and the 90 km s^{-1} cloud, are labeled by orange arrows in different panels where the mentioned structures are visible.

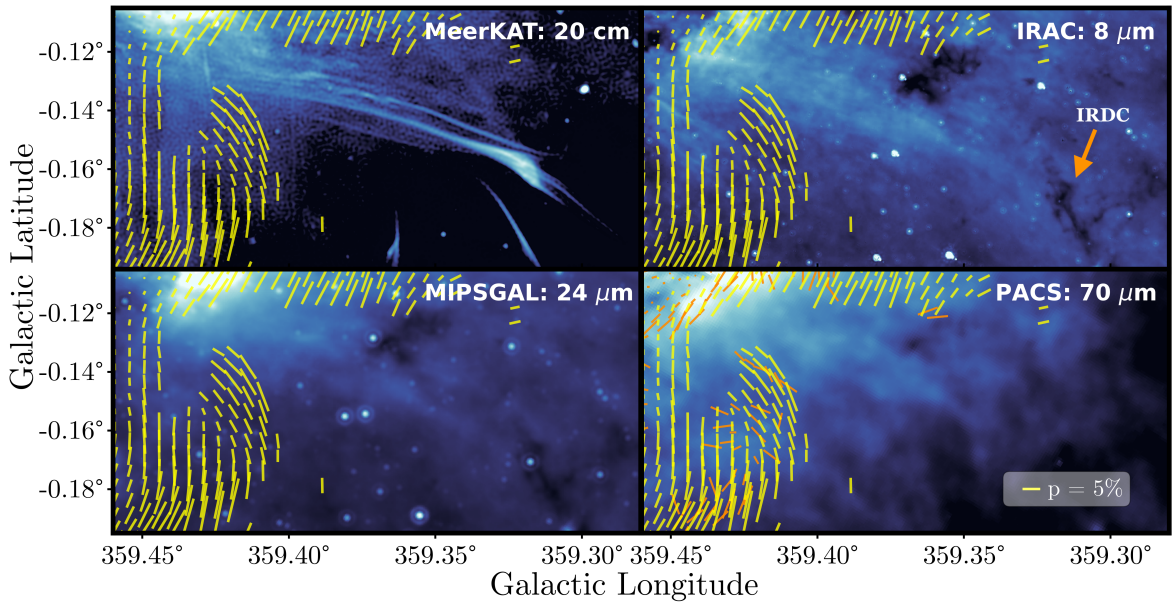


Figure 11. The G359.33-0.15 NTF toward the southwest of the Sgr C H II region shown at 20 cm (I. Heywood et al. 2022; F. Yusef-Zadeh et al. 2022b), 8 μm (S. Stolovy et al. 2006), 24 μm (S. J. Carey et al. 2009), and 70 μm (S. Molinari et al. 2010), overlaid with 214 μm magnetic field pseudovectors from D. Paré et al. (2024). The bright source in the top left corner in all four panels is the Sgr C H II region. The orange segments in the lower right panel are the 850 μm magnetic field detections from X. Lu et al. (2024). The location of an IRDC near $l = 359.^{\circ}32$, $b = -0.^{\circ}17$ is labeled by the orange arrow in the top right panel.

coincident with an extended X-ray source noted at energies <6 keV (which we detail in Section 5.2.2). Figure 11 shows the MeerKAT/*L*-Band image of the G359.33-0.15 filament bundle and its possible 8–70 μm counterparts. Such counterparts would be more characteristic of a thermal source rather than an NTF. However, the MeerKAT spectral index map (F. Yusef-Zadeh et al. 2022b; J. Bally et al. 2025) indicates that the spectrum of at least a portion of the G359.33-0.15 filaments is too steep to be thermal, although the mean spectral index is somewhat ambiguous in this regard. Furthermore, the multiplicity of the subfilaments is a characteristic commonly found among NTFs. Therefore, the apparent infrared counterparts to the G359.33-0.15 filaments could be coincidental and unrelated. No far-IR emission beyond 70 μm has been detected toward G359.33-0.15, and consequently, there are no 214 μm magnetic field detections to report along the G359.33-0.15 filaments.

Unlike most NTFs in the CMZ, which are perpendicular to the Galactic plane, the G359.33-0.15 filaments are much closer to being parallel to the Galactic plane. Another of its notable characteristics is that it is apparently interacting with an infrared dark cloud (IRDC) at its southwestern end (in the top two panels in Figure 11 at near $l = 359.^{\circ}32$, $b = -0.^{\circ}17$, and labeled by orange arrow in the top right panel), and that interaction has led to a strong morphological bunching and brightening of the radio emission at the interface (see Figure 3(k) of F. Yusef-Zadeh et al. 2022a for additional radio detail). The interaction has also led to the production of a slightly extended X-ray source at or very near that location (F. Yusef-Zadeh et al. 2007, their designation, G359.32-0.16), raising the possibility that this location is where the relativistic electrons that illuminate the G359.33-0.15 filament are produced, by an analogy with G359.1-0.2 (K. I. Uchida et al. 1996) or G0.18-0.04, and the Sickle (E. Serabyn & M. Morris 1994). This interesting structure clearly warrants further investigation. Unfortunately, no magnetic field detections have been measured along the G359.33-0.15 NTF and the IRDC with which it is interacting due to its low far-IR luminosity (FIREPLACE III).

5.1.4. Source C: G359.39-0.08

Source C is a radio source associated with a diffuse H II region to the immediate west of the Sgr C H II region, where thermal counterparts have been reported (H. S. Liszt & R. W. Spiker 1995; M. J. Hankins et al. 2020). Figure 12 displays multiwavelength structures of Source C overlaid with the 214 μm magnetic field pseudovectors, which exhibit a uniformly vertical structure with a similar polarization fraction. The magnetic field detections imply a low turbulent-to-ordered ratio and a largely uniform $|\boldsymbol{B}_{\rm POS}|$, as shown in Figure 5.

Source C contains a short radio filament with a bright southern end that ends abruptly at $l = 359.^{\circ}390$, $b = -0.^{\circ}077$ in the MeerKAT/L-Band image (labeled in the top left panel of Figure 12). To the northeast of that point, there are two adjacent and parallel filaments, the upper one of which appears to undergo a sudden northward deflection at $l = 359.^{\circ}405$, $b = -0.^{\circ}06$, above which its brightness increases. The deflection point of this filament is located within a far-IR emission cavity centered at $l = 359.^{\circ}405$, $b = -0.^{\circ}060$, where we find no significant magnetic field detection, but north of the cavity, the magnetic field orientation is approximately aligned with the filament. If the filament is a magnetic NTF, its "deflection" of the top filament could occur where it transitions going northward from the far-IR cavity into the local molecular cloud, thereby reflecting the differing field orientations in the two media.

Another notable feature in Source C is the curvature of the magnetic field around the peak of the 24 μm emission at $l = 359.^{\circ}37$, $b = -0.^{\circ}08$. This could perhaps be attributed to the expansion of the ionized gas in this region.

5.1.5. The Faint Southern Tail of the Sgr C NTF and Source G359.467-0.17

The prominent radio NTF extending north from Sgr C has an apparent faint southern "tail" that extends onto the -65 km s^{-1} cloud, in the projection, starting at $l = 359.^{\circ}468$, $b = -0.^{\circ}12$. The top left panel of Figure 13 shows the full extent of the Sgr C NTF, including the faint southern extension. It is apparent that there is a sharp decline in the brightness of the Sgr C NTF precisely where it overlaps with the head-tail cloud (depicted in yellow contours in the top left panel of Figure 13) on the sky-plane, suggesting that the NTF is interacting with the head-tail cloud. A zoomed-in view of the southern extension is shown in the top right panel of Figure 13. This tail is parallel to a bundle of other radio filaments having a more diffuse nature, shown in the top right panel of Figure 13 (see also Figure 12 of F. Yusef-Zadeh et al. 2022b). Additionally, we note the obvious spatial anticorrelation between this bundle of filaments with the PAH emission shown in 8 μm.

The NTF tail persists until $l = 359.^{\circ}[47$, $b = -0.^{\circ}25$. Along its trajectory, the tail is a tangent in the projection to a compact radio source, G359.467-0.17 (shown in detail in the bottom panel of Figure 13), which has the morphology of a tilted bipolar nebula, along with clear IR counterparts that indicate a centrally heated, dusty nebula. Because the brightness of the NTF tail does not vary as a function of its proximity to G359.467-0.17, it seems unlikely that the two structures are interacting.

5.2. The Sgr C H II Region

The $19.''6$ resolution of the FIREPLACE survey (FIREPLACE III) allows us to closely examine the magnetic field morphology near the Sgr C H II region. From Figure 3, we observe a cavity within the Sgr C H II region, in which relatively high-temperature dust resides, as manifested in mid-IR maps (panels (2)–(4) in Figure 7). In this paper, we focus on magnetic field detections in cold molecular clouds surrounding the H II region. Because such warm regions are not well sampled by our 214 μm survey, the field there would best be studied with future mid-IR polarimetry; indeed, a recent study by J. Bally et al. (2025) also inferred the existence of strong magnetic fields in this H II region, in the wavelength range 1–5 μm with JWST.

The magnetic field orientation in the northern hemisphere of the Sgr C H II region is mostly tangential to the radio shell shown in both Figure 3 and panel (9) of Figure 7. This tangential morphology along the northern surface of the H II region is consistent with the results of magnetohydrodynamic simulations (M. R. Krumholz et al. 2007; S. J. Arthur et al. 2011). We posit that the expanding shell of the H II region, presumably driven by stellar winds and the advancing ionization front, compresses the tangential component of the field in the surrounding clouds to the point where it has become the dominant component.

However, the magnetic field orientation near the head-tail cloud and the G359.44-0.10 EGO displays a different morphology. Near the EGO, the magnetic field is mainly influenced by activity in the EGO (protostellar winds and jets) instead of the ionization front of the Sgr C H II region, which is behind the head-tail cloud (C. C. Lang et al. 2010). We return to a more detailed discussion of the magnetic field morphology of the head-tail cloud in Section 5.3.

5.2.1. [C II] Emission: A "Shell" around the H II Region

To shed more light on the properties of the Sgr C H II region, we use the [C II] line analysis conducted by D. Riquelme et al. (2025, in preparation) using the upgraded German Receiver for Astronomy at Terahertz Frequencies

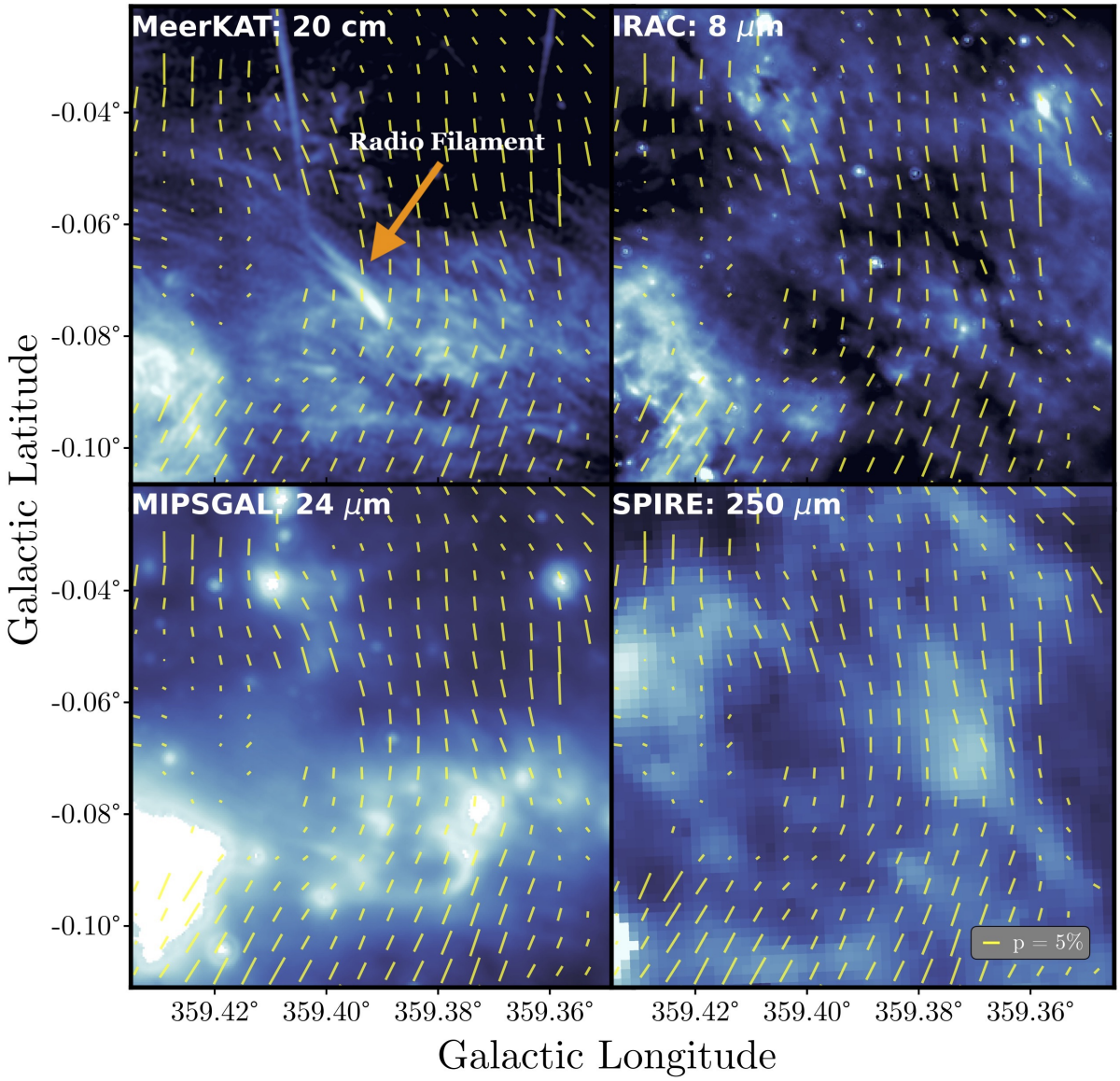


Figure 12. The FIREPLACE 214 μm magnetic field pseudovectors around Source C, superimposed on emission maps at 20 cm (I. Heywood et al. 2022), 8 μm (S. Stolovy et al. 2006), 24 μm (S. J. Carey et al. 2009), and 250 μm (S. Molinari et al. 2010). The yellow segments are the 214 μm magnetic field pseudovectors reported by D. Paré et al. (2024). No 850 μm magnetic field detections from X. Lu et al. (2024) were reported near Source C. The orange arrow labels the location of the radio filament near source C.

(upGREAT) instrument on board the SOFIA telescope. The [C II] line traces the warm ionized and partially ionized media exposed to UV photons from the H II region. Figure 14 displays the C II velocity channel image at -41 km s^{-1} (D. Riquelme et al. 2025, in preparation) overlaid by the FIREPLACE 214 μm magnetic field pseudovectors for comparison with the morphology of the C II shell. This particular velocity channel is chosen to best highlight the cavity structure revealed by the [C II] line. In the immediate vicinity of the Sgr C H II region, the 850 μm magnetic field measurements reported by X. Lu et al. (2024) are largely consistent with the 214 μm ones shown here.

Figure 14 reveals what appears to be a double-cavity morphology associated with the Sgr C H II region, with the western cavity being larger in size. The [C II] shell surrounds and overlaps with the outer perimeter of the H II region appearing in radio emission (see panel (9) in Figure 7), presumably identifiable as the ionization front. The 214 μm magnetic field orientation is mostly tangential to the cavities, except in the southeast direction because of the dense foreground head-tail cloud. The [C II] emission in this shell is found to deviate somewhat from circular symmetry, with the strongest emission in the northwest and near the G359.44-0.10 EGO. Together with the tangential magnetic field morphology, these observations resonate with the conclusion found in the simulations of S. J. Arthur et al. (2011) that the expansion of an H II region creates a tangential magnetic field orientation around its border. Moreover, the [C II] cavities are separated by a "bridge" of faint [C II] emission centered at $l = 359.^{\circ}455$, $b = -0.^{\circ}090$. Only two significant 214 μm pseudovectors are present toward the "bridge," and both are parallel to it.

The polarization fraction in high [C II] intensity regions appears low due to their high column density and high turbulent-to-ordered ratio, as shown in Section 3.2.1. Indeed, for the same region, the inferred $|\boldsymbol{B}_{\rm POS}|$ near the cavity is low.

T. R. Geballe et al. (2019) reported two dusty Wolf–Rayet stars that are located in the Sgr C H II region (pink-filled stars

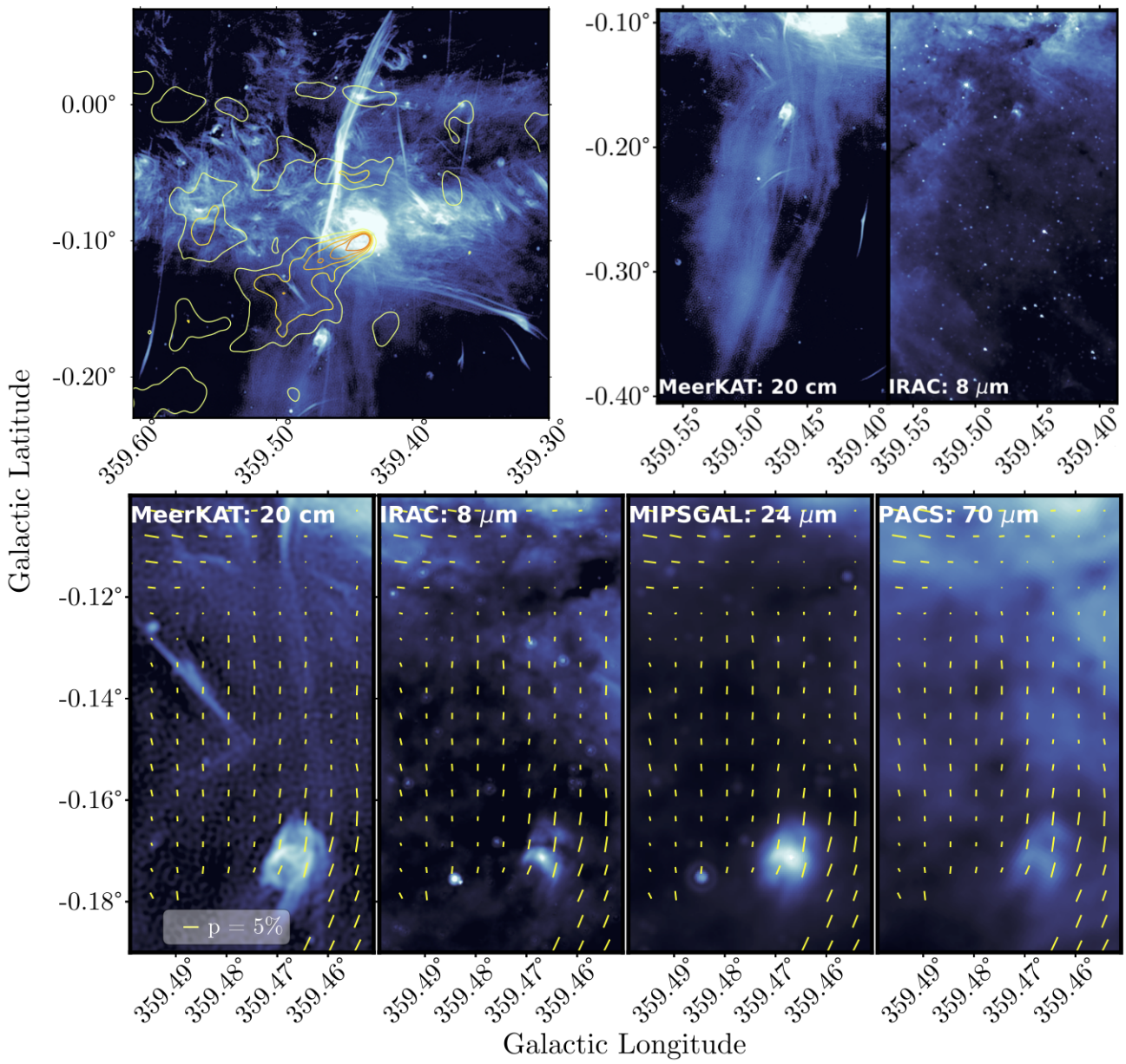


Figure 13. Top left: the full extent of the Sgr C NTF in radio continuum (I. Heywood et al. 2022). The orange contours are the FIREPLACE 214 μm emission at (3, 5.25, 7.5, 9.75, 12) Jy pixel^{-1} from D. Paré et al. (2024). Note the faint southern extension of the bright NTF bundle to the north. Top right: the faint southern "tail" of the Sgr C NTF, and source G359.467-0.17, displayed at wavelengths of 20 cm (I. Heywood et al. 2022) and 8 μm (S. Stolovy et al. 2006). Bottom: the extended 20 cm radio emission toward the south of the Sgr C H II region, from I. Heywood et al. (2022), 8 μm (S. Stolovy et al. 2006), 24 μm (S. J. Carey et al. 2009), and 70 μm (S. Molinari et al. 2010), overlaid with the 214 μm magnetic field pseudovectors from D. Paré et al. (2024).

in Figure 14). The western Wolf–Rayet star is positioned at the center of the western cavity, and is therefore a strong candidate for contributing to the formation of this cavity and to the ionization of the Sgr C H II region. Its winds are potentially responsible for the tangential magnetic field morphology around the rim of the Sgr C H II region.

5.2.2. X-Rays in the Sgr C H II Region

In projection, Sgr C is associated with an X-ray source having the spectroscopic and luminosity characteristics of a supernova remnant T. G. Tsuru et al. (2009). However, because the relatively low-resolution Suzaku observations reported by T. G. Tsuru et al. (2009) show that the peak X-ray emission in the 2.45 keV S XV Kα line is displaced from the Sgr C H II region, those authors conclude that the X-rays are unlikely to emanate from the H II region. A more recent observation by Q. D. Wang (2021) with Chandra resolves a secondary peak centred on the H II region, as shown in Figure 15, which overlays the 214 μm magnetic field pseudovectors on the 2.5–4 keV Chandra image.

This figure shows that the brightest portions of the secondary X-ray peak fit within the [C II] shell surrounding the H II region (white contour, from D. Riquelme et al. 2025, in preparation). Fainter X-ray emission extends away from the H II region both toward the northwest and to the southwest, where it extends continuously at a low level to the brightest X-ray peak lying ~2' (5 pc) from the H II region, at $l = 359.^{\circ}42$, b=-0.$^{\circ}$12. The two peaks of X-ray emission are possibly

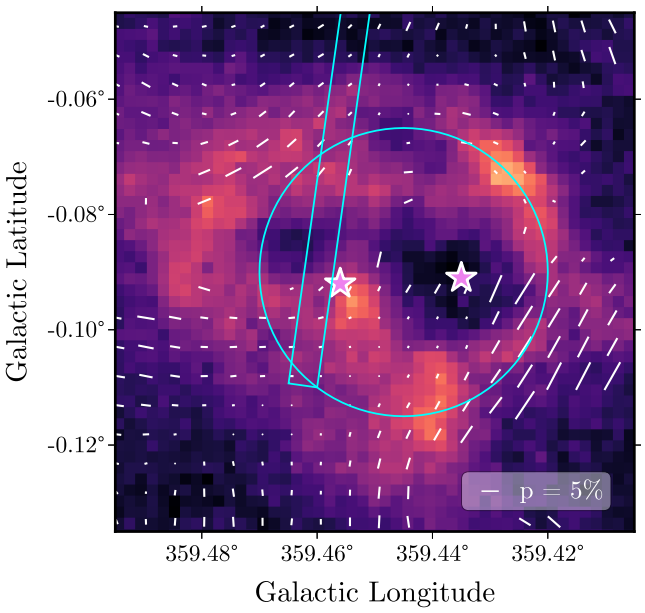


Figure 14. The CMZ in [C II] Survey image of the −41 km s^{-1} velocity channel observed using SOFIA/upGREAT (D. Riquelme et al. 2025, in preparation). White segments are the 214 μm pseudovectors made from data reported by D. Paré et al. (2024). Pink stars indicate the positions of two Wolf–Rayet stars reported by T. R. Geballe et al. (2019). The cyan schematics mark the approximate location and extent of the Sgr C H II region and the Sgr C NTF.

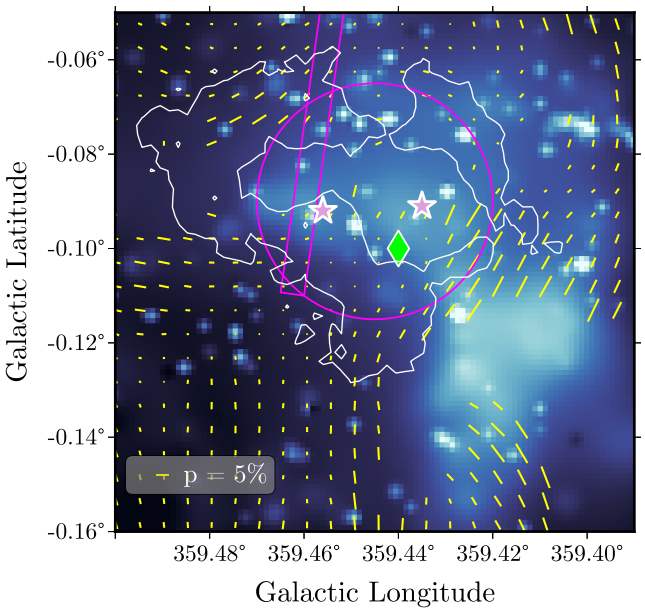


Figure 15. The 2.5–4 keV Chandra X-ray image reported by Q. D. Wang (2021). The white contour outlines the [C II] emission in the −41 km s^{-1} velocity channel at the intensity of 13 K (D. Riquelme et al. 2025, in preparation). The yellow segments are the 214 μm magnetic field pseudovectors made from D. Paré et al. (2024). The pink-filled star symbols mark the locations of two Wolf–Rayet stars (T. R. Geballe et al. 2019). The purple lines denote the location of the Sgr C H II region and the Sgr C NTF, and the green diamond indicates the location of the EGO at the "head" of the head-tail cloud.

connected through a ``bridge" at $l = 359.^{\circ}425$, b=-0.°103, although they could also be slightly overlapping, independent sources at different distances.If the X-rays from the secondary source arise from within the H II region, they could indicate that a supernova has taken place among the presumed cluster of massive stars that powers the H II region. The relative paucity of X-ray emission towards the southeast in the bands between 2.5–4 keV can perhaps be attributed to absorption by the head-tail cloud situated in front of the southeast portion of the H II region (T. Tsuru et al. 2009 also raised this same point to account for the shape of their X-ray contours at this location).

The stronger peak of extended X-ray emission to the southwest of the Sgr C H II region exhibits a strong spatial anti-correlation with far-IR emission and with the presence of significant 214 μm magnetic field detections (see Figure 3). We note again that the location of the X-ray emission to the southwest of the Sgr C H II region coincides in projection with the northeast ends of the G359.33-0.15 radio filaments (displayed in Figure 11 and detailed in Section 5.1.3), although it is not yet clear whether there is any physical association between these two features.

5.3. The Head-tail Cloud (G359.44-0.10) and the −65 km s^{-1} Cloud

To the southeast of the Sgr C H II region lies the head-tail cloud. The head-tail cloud consists of two parts: an exceptionally bright compact source (the G359.43-0.10 EGO or the "head"; S. Kendrew et al. 2013; S. Crowe et al. 2024; green star in the lower left panel of Figure 16) and a diffuse and cometary ridge of high far-IR luminosity, high column density (see Figure 6), and low polarization fraction extending toward the southeast (the "tail" addressed in Section 5.1.5). This cloud is also found to exhibit a consistently high turbulent-to-ordered ratio ($\langle \boldsymbol{B}_t^2 \rangle / \langle \boldsymbol{B}_0^2 \rangle$), as detailed in Section 3.2.1. Figure 16 shows the magnetic field pseudovectors of the head-tail cloud and the −65 km s^{-1} cloud overlaid with various background images. Initially discovered by J. R. Forster & J. L. Caswell (2000) and F. Yusef-Zadeh et al. (2009), S. Kendrew et al. (2013) confirm the existence of early stage star formation within the EGO, driving multiple jetlike protostellar outflows, recently detailed by S. Crowe et al. (2024). These magnetic field orientations can be due to the cloud being sheared along its long dimension. Alternatively, the head-tail cloud is moving as a unit with constant velocity, and the magnetic field lines threading through that cloud, originally roughly perpendicular to the cloud, can be deformed and dragged into their observed orientations by the bulk motion of the cloud, into which the field lines are frozen. Toward the southeast of the EGO, the tail forms a coherent structure continuous with the −65 km s^{-1} cloud, as depicted in Figure 8.

The JCMT/POL2 polarimetric study surveyed this region at 850 μm (X. Lu et al. 2024; shown in orange in the lower left panel of Figure 16). We note that the 850 μm magnetic field pseudovector orientations near the "head" generally agree with those of FIREPLACE III. However, in the body of the −65 km s^{-1} cloud near $l = 359.^{\circ}47$, $b = -0.^{\circ}16$ (purple rectangle in the lower left of Figure 16), there are several 850 μm magnetic field detections, which appear roughly parallel to the Galactic plane and perpendicular to those detected at 214 μm. This misalignment could occur if the polarimetric surveys at different wavelengths are detecting emission from different temperature regimes within the clouds or different components of the same cloud along a given line of sight.

Furthermore, we outline a few intriguing morphological associations between the 214 μm magnetic field pseudovectors and several observed structures in the −65 km s^{-1} cloud, shown in Figure 17. The magnetic field within the −65 km s^{-1} cloud is separable into three distinct parts, whose spatial extent is well represented by regions #1, #2, and #4 of the

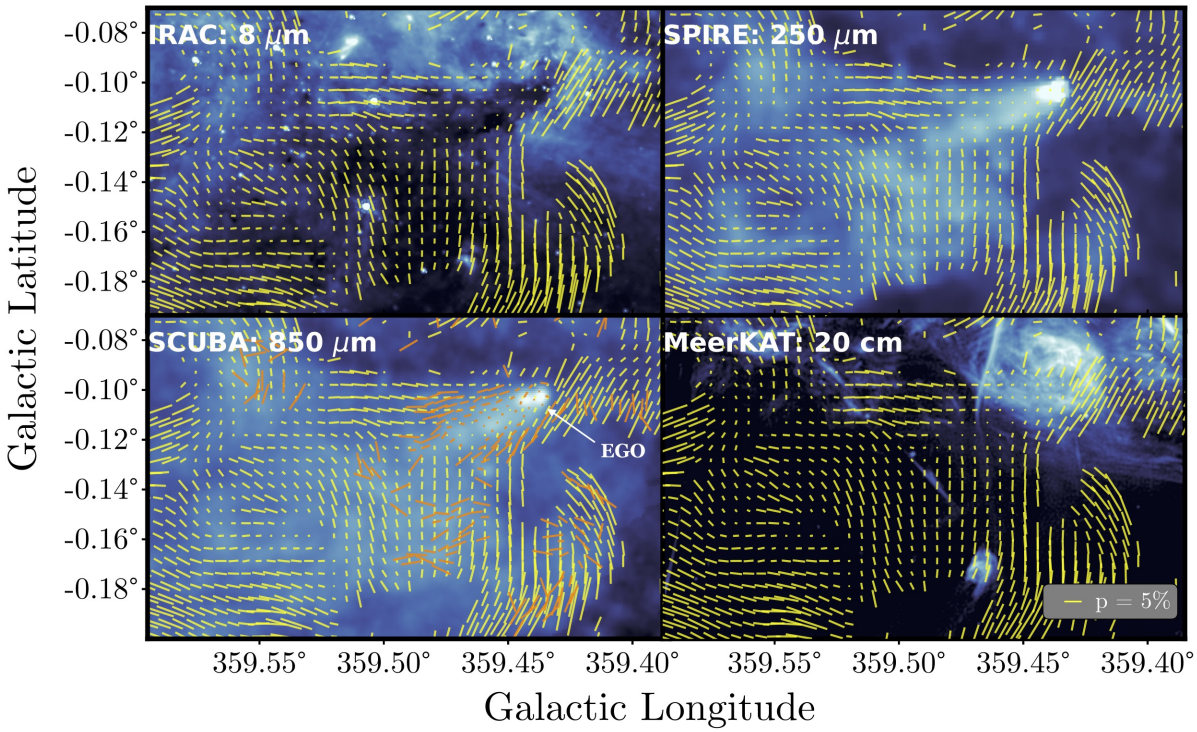


Figure 16. The magnetic field pseudovector representation from FIREPLACE coinciding with the head-tail cloud and the −65 km s^{-1} cloud, displayed at wavelengths of 8 μm (S. Stolovy et al. 2006), 250 μm (S. Molinari et al. 2010), 850 μm (D. Pierce-Price et al. 2000), and 20 cm (I. Heywood et al. 2022). The orange pseudovectors in the lower left panel are the 850 μm magnetic field pseudovectors from X. Lu et al. (2024). The purple rectangle in the lower left panel denotes the extent of source AGAL 359.474-0.152 detected in the 870 μm ATLASGAL survey (Y. Contreras et al. 2013). The white arrow in the lower left panel labels the location of the EGO.

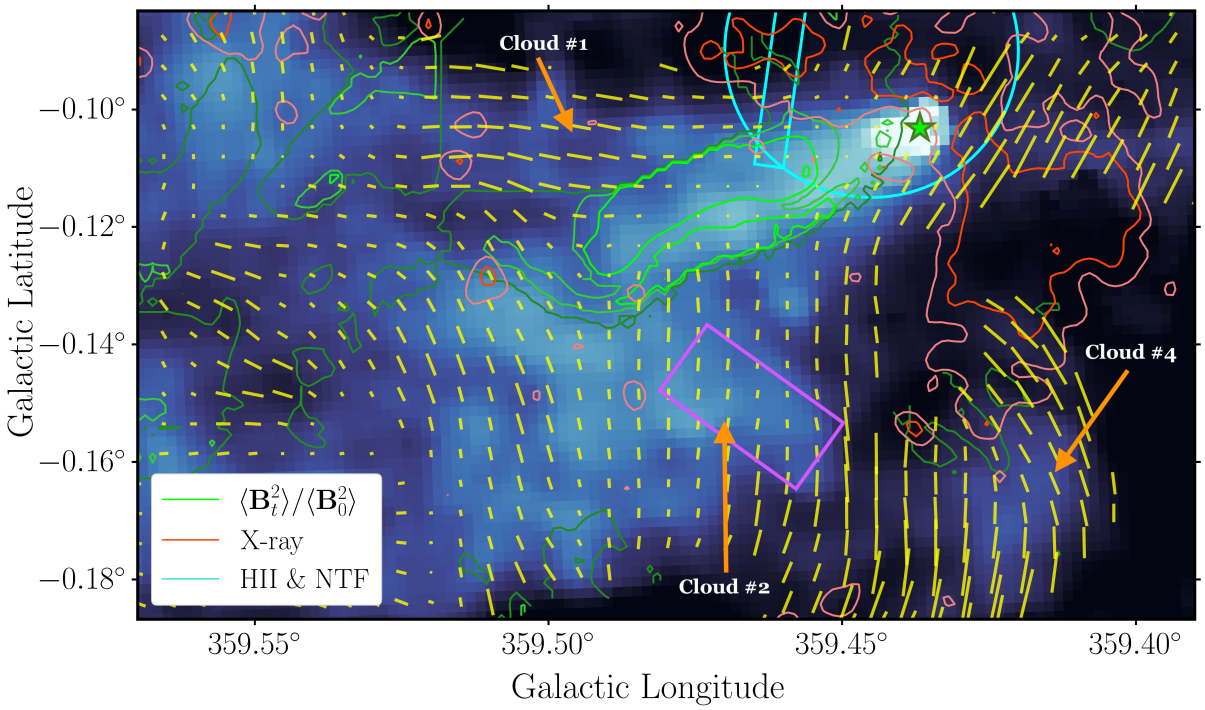


Figure 17. Various morphological features within the −65 km s^{-1} cloud. The yellow segments are the 214 μm magnetic field pseudovectors from D. Paré et al. (2024), superposed upon the Herschel/SPIRE 250 μm intensity image. The green contours are the $\langle \boldsymbol{B}_t^2 \rangle / \langle \boldsymbol{B}_0^2 \rangle$ ratio at values of (0.1, 0.6, 1.2). The red contours depict the 2.5–4 keV X-ray intensity from Q. D. Wang (2021) at (5000, 7000) counts s^{-1} arcmin^{-2}. The cyan outlines indicate the extent of the Sgr C H II region and the Sgr C NTF. The purple rectangle denotes the extent of source AGAL 359.474-0.152 detected in the 870 μm ATLASGAL survey (Y. Contreras et al. 2013). The green star labels the location of the EGO. The orange arrows label the extent of Clouds #1, #2, and #4 in Figure 4 used in the DCF analysis in Section 3.2.

$-65\,\mathrm{km\,s^{-1}}$ cloud in Figure 4. In this subsection, we continue to adopt this naming scheme for our discussion, and in the following, we summarize the magnetic field morphology of each region, and describe potential relationships with structures observed at other wavelengths:

1. *Cloud #1*. This cloud, centered at $l = 359.^{\circ}495$, $b = -0.^{\circ}11$, lies between the Galactic plane to the north (the far-IR-dark region near the top of Figure 16) and the high turbulent-to-ordered ratio "ridge" (the green contours in Figure 16) in the south. X. Lu et al. (2024) argue that the field morphology in this region, which is parallel to the Galactic plane, is due to its interaction with numerous H II regions along the Galactic plane (S. J. Carey et al. 2009; M. J. Hankins et al. 2020).
2. *Cloud #2*. This cloud, centered at $l = 359.^{\circ}47$, $b = -0.^{\circ}15$, is located to the south of Cloud #1, bordered by the high turbulent-to-ordered ratio "ridge" to the north and the 2.5–4 keV X-ray emission source to the west (orange contours in Figure 17). The magnetic field within Cloud #2 is uniformly perpendicular to the Galactic plane and to the magnetic field orientation observed in Cloud #1. However, the magnetic field transition from Cloud #1 to Cloud #2 takes place toward the high turbulent-to-ordered ratio "ridge," thus obscuring the transition from our perspective. We note additionally that the SiO emission in Figure 9 is exclusively found in Cloud #2, likely supporting the case that the magnetic field systems in these listed clouds are segregated.
3. *Cloud #4*. Centered at $l = 359.^{\circ}425$, $b = -0.^{\circ}17$, Cloud #4 is separated from Cloud #2 above $b = -0.^{\circ}15$ but merges with Cloud #2 below this latitude. We note that the far-IR "gulf" approximately located at $l = 359.^{\circ}43$, $b = -0.^{\circ}14$ exhibits an intriguing spatial anticorrelation with the 2.5–4 keV X-ray emission (orange contours in Figure 17). FIREPLACE III argues that the curved magnetic field morphology of Cloud #4 can possibly be ascribed to winds associated with star formation in the aforementioned 870 μm source AGAL 359.474-0.152 (Y. Contreras et al. 2013).

We note that the observation we provided in this section only pertains to the 214 μm magnetic field measurements. For instance, we do not take into account the observed JCMT/POL2 pseudovectors in Cloud #2 (X. Lu et al. 2024). However, we note again that the JCMT/POL2 measurements may be sampling from a different temperature regime or another cloud along the same line of sight. A multiwavelength dust polarimetry measurement that covers a larger area is warranted to properly interpret the observational differences at the two wavelengths.

6. Conclusion

This paper presents a detailed analysis of the FIREPLACE magnetic field measurements from the FIREPLACE dust polarimetry survey (FIREPLACE III) in the Sgr C complex.

We summarize our findings as follows:

1. As was reported in the earlier FIREPLACE papers (FIREPLACE I; FIREPLACE III; FIREPLACE IV), we find that the polarization fraction exhibits an anticorrelation with 214 μm intensity. As such, the polarization fraction on the boundary of clouds is typically higher than in the center of clouds. The higher polarization fraction is likely a result of a combination of two effects: (1) decreased turbulence toward the boundary of clouds, as indicated by our angular dispersion analysis, and (2) by the likelihood that the multiplicity of different magnetic domains within the cloud is likely to be smaller toward the edges of clouds.
2. Through a modified DCF analysis of individual clouds, we find the sky-plane magnetic field strength to be 30 μG–1 mG in Sgr C. Regions with higher turbulence typically have weaker magnetic field strength, such as the head-tail cloud and near the Sgr C H II region. The dominant determinant of the plane-of-sky magnetic field strength is the local turbulence.
3. The expansion of the Sgr C H II region causes extensive turbulent behavior in its vicinity, as shown by our DCF analysis. We find that the H II region's interior has been cleared of cold dust content since no far-IR emission is seen there, thereby creating a cavity devoid of significant 214 μm magnetic field pseudovectors. Additionally, we find that the 214 magnetic field orientation is largely tangential to the [C II] shell surrounding the H II region reported by D. Riquelme et al. (2025, in preparation), and briefly shown in Figure 14. The angular dispersion analysis again confirms the elevated turbulence in this shell, accompanied by existing molecular shock tracers. We note an intriguing diffuse source of X-ray emission to the southwest of the Sgr C H II region, which warrants further study as potentially resulting from past activity in the Sgr C region.
4. The magnetic field morphology near the base of the Sgr C NTF is consistent with the hypotheses that either magnetic field line reconnection or diffusive shock acceleration at the ionization/compression front of the H II region is responsible for the relativistic electrons that illuminate the NTF with their synchrotron emission. Also, the field direction in the $-90\,\mathrm{km\,s^{-1}}$ cloud is found to be parallel to the filament.
5. We have examined the morphological correspondences between the 214 and 850 μm magnetic field pseudovectors and numerous radio features, such as Source C, FIR-4, and the G359.33-0.15 filaments. From these comparisons, we conclude that many radio structures in the Sgr C region exhibit morphological correspondences with the observed magnetic field direction. Future multiwavelength dust polarimetry surveys, coupled with detailed molecular line surveys, are needed to elucidate the dynamics of these structures and to determine how the magnetic field and the gas are interacting.

7. Acknowledgments

This work is primarily based on observations made with the NASA/DLR Stratospheric Observatory for Infrared Astronomy (SOFIA). SOFIA was jointly operated by the Universities Space Research Association, Inc. (USRA), under NASA contract NNA17BF53C, and the Deutsches SOFIA Institut (DSI) under DLR contract 50 OK 2002 to the University of Stuttgart.

Financial support for this work was provided by NASA through award No. 09-0054 through USRA. This work has made extensive use of NASA's Astrophysics Data System (http://ui.adsabs.harvard.edu/) and the arXiv e-Print service (http://arxiv.org). In addition, part of this work is completed using the computing resources provided by the University of Chicago's Research Computing Center. Publication of this work is in part

supported by the National Radio Astronomy Observatory. The National Radio Astronomy Observatory and Green Bank Observatory are facilities of the U.S. National Science Foundation operated under cooperative agreement by Associated Universities, Inc.

R.J.Z. and M.R.M. are supported by NASA through award No. 09-0054 administered as a subgrant to UCLA. R.J.Z. thanks Keila Cunha e Silva and Joan-Emma Shea for generously sharing their computing resources, and Q. Daniel Wang for kindly providing his data. Finally, R.J.Z. wishes to acknowledge all community members of Meadowridge School, located in British Columbia, Canada, for their homelike hospitality, helpful conversations, and immense kindness while much of this work was completed.

The authors at UCLA Department of Physics & Astronomy acknowledge our presence on the traditional, ancestral, and unceded territory of the Gabrielino/Tongva peoples. Much of this work was completed at Meadowridge School, located on the ancestral and unceded territories of the Katzie, Kwantlen, and Coast Salish Peoples, as well as the University of Chicago, located on the ancestral and unceded territories of the Kickapoo, Peoria, Potawatomi, Miami, and Sioux people. We value the opportunity to learn, live, and share research and educational experiences on these traditional lands.

Facilities: SOFIA, CXO, Herschel, JCMT, MeerKAT, Mopra, Spitzer.

Software: ASTROPY (Astropy Collaboration et al. 2013, 2018), CASA (CASA Team et al. 2022), CMOCEAN (K. M. Thyng et al. 2016), EMCEE (D. Foreman-Mackey et al. 2013), MATPLOTLIB (J. D. Hunter 2007), NUMPY (C. R. Harris et al. 2020), PANDAS (The pandas development team 2020), POLBPY (J. A. Guerra et al. 2024), SCIPY (P. Virtanen et al. 2020).

Appendix
Autocorrelation Function of Sgr C Clouds

In this section, we present more details of the autocorrelation function computation and effective cloud depth. We show the shapes of the autocorrelation function calculated for the individual Sgr C clouds in Figure A1. We refer the readers to Figure 4 for the location and extent of individual regions. The

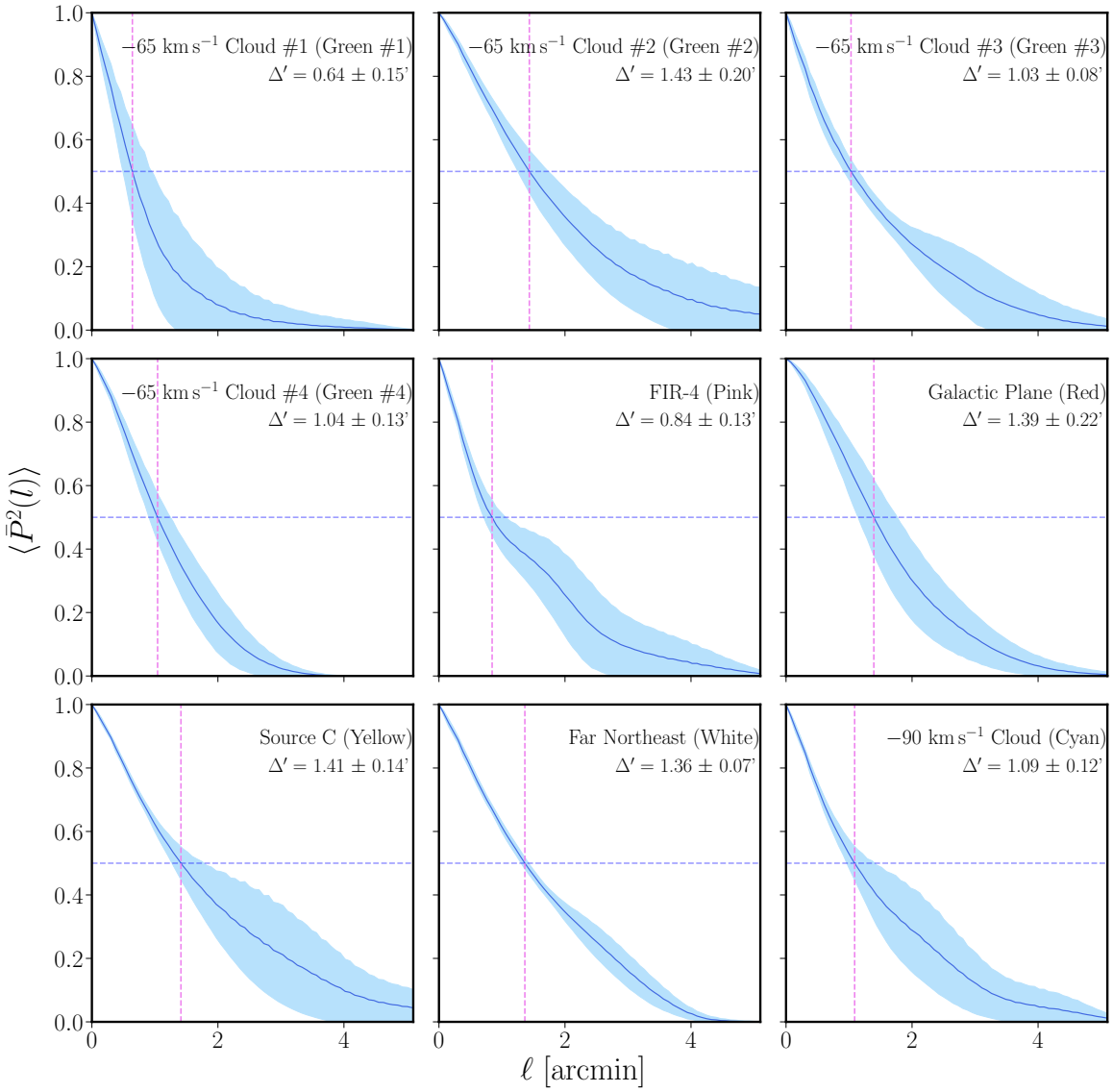


Figure A1. The autocorrelation functions computed from individual Sgr C clouds, as defined in Figure 4. The blue curves are the autocorrelation functions ($\langle \bar{P}^2(l) \rangle$), and the shaded region indicate the standard error. The purple horizontal line indicates where $\langle \bar{P}^2(l) \rangle = 0.5$. The burgundy vertical line indicates the HWHM value of the autocorrelation function, which is equivalent to the effective cloud depth.

cloud depth is positively correlated with the size and uniformity of a region. The autocorrelation functions typically exhibit a monotonic decline, except for FIR-4 where a "bump" near $l \approx 1.'4$ is observed (central panel). The shape of the FIR-4 autocorrelation function is likely a result of its morphology. The vertical extent of FIR-4 is roughly $1.'4$ or $0.^{\circ}02$; therefore, the autocorrelation function likely displays the increase of polarized flux toward the northern and southern periphery of FIR-4.

ORCID iDs

Roy J. Zhao https://orcid.org/0009-0001-9716-4188
Mark R. Morris https://orcid.org/0000-0002-6753-2066
David T. Chuss https://orcid.org/0000-0003-0016-0533
Dylan M. Paré https://orcid.org/0000-0002-5811-0136
Jordan A. Guerra https://orcid.org/0000-0001-8819-9648
Natalie O. Butterfield https://orcid.org/0000-0002-4013-6469
Edward J. Wollack https://orcid.org/0000-0002-7567-4451
Kaitlyn Karpovich https://orcid.org/0009-0006-4830-163X

References

Aitken, D. K., Gezari, D., Smith, C. H., McCaughrean, M., & Roche, P. F. 1991, ApJ, 380, 419
Aitken, D. K., Smith, C. H., Moore, T. J. T., & Roche, P. F. 1998, MNRAS, 299, 743
Akshaya, M. S., & Hoang, T. 2024, MNRAS, 531, 5012
Andersson, B. G., Lazarian, A., & Vaillancourt, J. E. 2015, ARA&A, 53, 501
Arendt, R. G., Staguhn, J., Dwek, E., et al. 2019, ApJ, 885, 71
Arthur, S. J., Henney, W. J., Mellema, G., de Colle, F., & Vázquez-Semadeni, E. 2011, MNRAS, 414, 1747
Astropy Collaboration, Price-Whelan, A. M., Sipőcz, B. M., et al. 2018, AJ, 156, 123
Astropy Collaboration, Robitaille, T. P., Tollerud, E. J., et al. 2013, A&A, 558, A33
Bally, J., Crowe, S., Fedriani, R., et al. 2025, ApJ, 983, 20
Banda-Barragán, W. E., Federrath, C., Crocker, R. M., & Bicknell, G. V. 2018, MNRAS, 473, 3454
Banda-Barragán, W. E., Parkin, E. R., Federrath, C., Crocker, R. M., & Bicknell, G. V. 2016, MNRAS, 455, 1309
Battersby, C., Bally, J., Ginsburg, A., et al. 2011, A&A, 535, A128
Battersby, C., Walker, D. L., Barnes, A., et al. 2025, ApJ, 984, 156
Boldyrev, S., & Yusef-Zadeh, F. 2006, ApJL, 637, L101
Bryant, A., & Krabbe, A. 2021, NewAR, 93, 101630
Butterfield, N. O., Chuss, D. T., Guerra, J. A., et al. 2024a, ApJ, 963, 130
Butterfield, N. O., Guerra, J. A., Chuss, D. T., et al. 2024b, ApJ, 968, 63
Cabral, B., & Leedom, L. C. 1993, in Proc. 20th Annual Conf. on Computer Graphics and Interactive Techniques, ed. M. C. Whitton (New York: ACM), 263
Carey, S. J., Noriega-Crespo, A., Mizuno, D. R., et al. 2009, PASP, 121, 76
CASA Team, Bean, B., Bhatnagar, S., et al. 2022, PASP, 134, 114501
Chandrasekhar, S., & Fermi, E. 1953, ApJ, 118, 113
Chuss, D. T., Andersson, B. G., Bally, J., et al. 2019, ApJ, 872, 187
Chuss, D. T., Davidson, J. A., Dotson, J. L., et al. 2003, ApJ, 599, 1116
Compiègne, M., Flagey, N., Noriega-Crespo, A., et al. 2010, ApJL, 724, L44
Contreras, Y., Schuller, F., Urquhart, J. S., et al. 2013, A&A, 549, A45
Cotera, A. S., Hankins, M. J., Bally, J., et al. 2024, ApJ, 973, 110
Crocker, R. M., Jones, D. I., Melia, F., Ott, J., & Protheroe, R. J. 2010, Natur, 463, 65
Crowe, S., Fedriani, R., Tan, J. C., et al. 2024, ApJ, 983, 19
Davis, L. 1951, PhRv, 81, 890
Downes, D., & Maxwell, A. 1966, ApJ, 146, 653
Ferrière, K. 2009, A&A, 505, 1183
Ferrière, K., Gillard, W., & Jean, P. 2007, A&A, 467, 611
Foreman-Mackey, D., Conley, A., Meierjurgen Farr, W., et al., 2013 emcee: The MCMC Hammer, Astrophysics Source Code Library, ascl:1303.002
Forster, J. R., & Caswell, J. L. 2000, ApJ, 530, 371
Geballe, T. R., Lambrides, E., Schlegelmilch, B., et al. 2019, ApJ, 872, 103
Gordon, M. S., Lopez-Rodriguez, E., Andersson, B. G., et al. 2018, arXiv:1811.03100
GRAVITY Collaboration, Abuter, R., Amorim, A., et al. 2019, A&A, 625, L10
Guan, Y., Clark, S. E., Hensley, B. S., et al. 2021, ApJ, 920, 6
Guerra, J. A., Chuss, D. T., Dowell, C. D., et al. 2021, ApJ, 908, 98
Guerra, J. A., Chuss, D. T., & Paré, D. 2024, polBpy: A Python Package for the Analysis of Dust Polarimetric Observations, Version 0.1.2, Zenodo, doi:10.5281/zenodo.11414008.2024
Guerra, J. A., Lopez-Rodriguez, E., Chuss, D. T., Butterfield, N. O., & Schmelz, J. T. 2023, AJ, 166, 37
Hankins, M. J., Lau, R. M., Morris, M. R., & Herter, T. L. 2017, ApJ, 837, 79
Hankins, M. J., Lau, R. M., Radomski, J. T., et al. 2020, ApJ, 894, 55
Harper, D. A., Runyan, M. C., Dowell, C. D., et al. 2018, JAI, 7, 1840008
Harris, C. R., Millman, K. J., van der Walt, S. J., et al. 2020, Natur, 585, 357
Henshaw, J. D., Barnes, A. T., Battersby, C., et al. 2023, in ASP Conf. Ser. 534, Protostars and Planets VII, ed. S. Inutsuka et al. (San Francisco, CA: ASP), 83
Heywood, I., Rammala, I., Camilo, F., et al. 2022, ApJ, 925, 165
Hildebrand, R. H., Kirby, L., Dotson, J. L., Houde, M., & Vaillancourt, J. E. 2009, ApJ, 696, 567
Houde, M., Hull, C. L. H., Plambeck, R. L., Vaillancourt, J. E., & Hildebrand, R. H. 2016, ApJ, 820, 38
Houde, M., Vaillancourt, J. E., Hildebrand, R. H., Chitsazzadeh, S., & Kirby, L. 2009, ApJ, 706, 1504
Hsieh, P.-Y., Koch, P. M., Kim, W.-T., et al. 2018, ApJ, 862, 150
Hunter, J. D. 2007, CSE, 9, 90
Jones, P. A., Burton, M. G., Cunningham, M. R., et al. 2012, MNRAS, 419, 2961
Kendrew, S., Ginsburg, A., Johnston, K., et al. 2013, ApJL, 775, L50
Kruijssen, J. M. D., Longmore, S. N., Elmegreen, B. G., et al. 2014, MNRAS, 440, 3370
Krumholz, M. R., & Kruijssen, J. M. D. 2015, MNRAS, 453, 739
Krumholz, M. R., Stone, J. M., & Gardiner, T. A. 2007, ApJ, 671, 518
Lang, C. C., Goss, W. M., Cyganowski, C., & Clubb, K. I. 2010, ApJS, 191, 275
LaRosa, T. N., Brogan, C. L., Shore, S. N., et al. 2005, ApJL, 626, L23
Liszt, H. S. 1985, ApJL, 293, L65
Liszt, H. S., & Spiker, R. W. 1995, ApJS, 98, 259
Lu, X., Li, S., Ginsburg, A., et al. 2021, ApJ, 909, 177
Lu, X., Liu, J., Pillai, T., et al. 2024, ApJ, 962, 39
Lu, X., Mills, E. A. C., Ginsburg, A., et al. 2019, ApJS, 244, 35
Mangilli, A., Aumont, J., Bernard, J. P., et al. 2019, A&A, 630, A74
Molinari, S., Bally, J., Noriega-Crespo, A., et al. 2011, ApJL, 735, L33
Molinari, S., Schisano, E., Elia, D., et al. 2016, A&A, 591, A149
Molinari, S., Swinyard, B., Bally, J., et al. 2010, PASP, 122, 314
Morris, M. 1993, ApJ, 408, 496
Morris, M. 1996, in IAU Symp. 169, ed. L. Blitz & P. J. Teuben (Dordrecht: Kluwer), 247
Morris, M. 2006, JPhCS, 54, 1
Morris, M., Davidson, J. A., Werner, M., et al. 1992, ApJL, 399, L63
Morris, M., & Serabyn, E. 1996, ARA&A, 34, 645
Morris, M., & Yusef-Zadeh, F. 1985, AJ, 90, 2511
Morris, M. R. 2015, in Lessons from the Local Group: A Conf. in honor of David Block and Bruce Elmegreen, ed. K. Freeman et al. (Cham: Springer), 391
Morris, M. R. 2023, in Physics and Chemistry of Star Formation: The Dynamical ISM Across Time and Spatial Scales. Proc. of the 7th Chile-Cologne-Bonn Symp., ed. V. Ossenkopf-Okada et al. (Cologne: Universitäts- und Stadtbibliothekj Köln), 49
Narayanan, D., Smith, J. D. T., Hensley, B. S., et al. 2023, ApJ, 951, 100
Novak, G., Chuss, D. T., Renbarger, T., et al. 2003, ApJL, 583, L83
Novak, G., Dotson, J. L., Dowell, C. D., et al. 2000, ApJ, 529, 241
Odenwald, S. F., & Fazio, G. G. 1984, ApJ, 283, 601
Paré, D., Butterfield, N. O., Chuss, D. T., et al. 2024, ApJ, 969, 150
Paré, D. M., Chuss, D. T., Karpovich, K., et al. 2025, ApJ, 978, 28
Parker, E. N. 1979, Cosmical Magnetic Fields. Their Origin and Their Activity (Oxford: Clarendon Press)
Pierce-Price, D., Richer, J. S., Greaves, J. S., et al. 2000, ApJL, 545, L121
Pillai, T., Kauffmann, J., Tan, J. C., et al. 2015, ApJ, 799, 74
Planck Collaboration, Ade, P. A. R., Aghanim, N., et al. 2015, A&A, 576, A104
Rosner, R., & Bodo, G. 1996, ApJL, 470, L49
Roy, S. 2003, A&A, 403, 917
Sadavoy, S. I., Di Francesco, J., Johnstone, D., et al. 2013, ApJ, 767, 126
Salas, J. M., Naoz, S., & Morris, M. R. 2020, arXiv:2010.04170
Schuller, F., Menten, K. M., Contreras, Y., et al. 2009, A&A, 504, 415
Serabyn, E., & Morris, M. 1994, ApJL, 424, L91

Sormani, M. C., Sobacchi, E., Fragkoudi, F., et al. 2018, MNRAS, 481, 2
Sormani, M. C., Sobacchi, E., & Sanders, J. L. 2024, MNRAS, 528, 5742
Sormani, M. C., Tress, R. G., Glover, S. C. O., et al. 2020, MNRAS, 497, 5024
Stolovy, S., Ramirez, S., Arendt, R. G., et al. 2006, JPhCS, 54, 176
The pandas development team 2020, pandas-dev/pandas: Pandas, Version 1.5.3, Zenodo, doi:10.5281/zenodo.3509134
Thomas, T., Pfrommer, C., & Enßlin, T. 2020, ApJL, 890, L18
Thyng, K. M., Greene, C. A., Hetland, R. D., Zimmerle, H. M., & DiMarco, S. F. 2016, Ocgpy, 29, 9
Tress, R. G., Sormani, M. C., Girichidis, P., et al. 2024, A&A, 691, A303
Tsuboi, M., Inoue, M., Handa, T., Tabara, H., & Kato, T. 1985, PASJ, 37, 359
Tsuru, T. G., Nobukawa, M., Nakajima, H., et al. 2009, PASJ, 61, S219
Uchida, K., Morris, M., & Serabyn, E. 1990, ApJ, 351, 443
Uchida, K. I., Morris, M., Serabyn, E., & Guesten, R. 1996, ApJ, 462, 768
Uchida, K. I., Morris, M. R., Serabyn, E., & Bally, J. 1994, ApJ, 421, 505
Vaillancourt, J. E. 2002, ApJS, 142, 53
Virtanen, P., Gommers, R., Oliphant, T. E., et al. 2020, NatMe, 17, 261
Wang, Q. D. 2021, MNRAS, 504, 1609
Wardle, M., & Konigl, A. 1990, ApJ, 362, 120
Werner, M. W., Davidson, J. A., Morris, M., et al. 1988, ApJ, 333, 729
Yusef-Zadeh, F., Arendt, R. G., Wardle, M., Heywood, I., & Cotton, W. 2022a, MNRAS, 517, 294
Yusef-Zadeh, F., Arendt, R. G., Wardle, M., et al. 2022b, MNRAS, 515, 3059
Yusef-Zadeh, F., Arendt, R. G., Wardle, M., et al. 2022c, ApJL, 925, L18
Yusef-Zadeh, F., Hewitt, J. W., Arendt, R. G., et al. 2009, ApJ, 702, 178
Yusef-Zadeh, F., & Königl, A. 2004, in ASP Conf. Ser. 322, The Formation and Evolution of Massive Young Star Clusters (San Francisco, CA: ASP), 201
Yusef-Zadeh, F., Morris, M., & Chance, D. 1984, Natur, 310, 557
Yusef-Zadeh, F., Muno, M., Wardle, M., & Lis, D. C. 2007, ApJ, 656, 847
Yusef-Zadeh, F., Roberts, D. A., Goss, W. M., Frail, D. A., & Green, A. J. 1999, ApJ, 512, 230
Yusef-Zadeh, F., & Wardle, M. 2019, MNRAS, 490, L1